

# Nucleon electromagnetic form factors from lattice QCD using a nearly physical pion mass

J. R. Green,<sup>\*</sup> J. W. Negele, and A. V. Pochinsky

*Center for Theoretical Physics, Massachusetts Institute of Technology, Cambridge, Massachusetts 02139, USA*

S. N. Syritsyn<sup>†</sup>

*Nuclear Science Division, Lawrence Berkeley National Laboratory, Berkeley, California 94720, USA*

M. Engelhardt

*Department of Physics, New Mexico State University, Las Cruces, NM 88003-8001, USA*

S. Krieg

*Bergische Universität Wuppertal, D-42119 Wuppertal, Germany and*

*IAS, Jülich Supercomputing Centre, Forschungszentrum Jülich, D-52425 Jülich, Germany*

(Dated: November 20, 2014)

We present lattice QCD calculations of nucleon electromagnetic form factors using pion masses  $m_\pi = 149, 202$ , and  $254$  MeV and an action with clover-improved Wilson quarks coupled to smeared gauge fields, as used by the Budapest-Marseille-Wuppertal collaboration. Particular attention is given to removal of the effects of excited state contamination by calculation at three source-sink separations and use of the summation and generalized pencil-of-function methods. The combination of calculation at the nearly physical mass  $m_\pi = 149$  MeV in a large spatial volume ( $m_\pi L_s = 4.2$ ) and removal of excited state effects yields agreement with experiment for the electric and magnetic form factors  $G_E(Q^2)$  and  $G_M(Q^2)$  up to  $Q^2 = 0.5$  GeV<sup>2</sup>.

PACS numbers: 12.38.Gc, 13.40.Gp

Keywords: form factors, lattice QCD, hadron structure

## I. INTRODUCTION

Electromagnetic form factors are of great interest theoretically and experimentally because they specify fundamental aspects of the structure of nucleons. At low momentum transfer, they reveal the spatial distribution of charge and current. In a non-relativistic system, the electric and magnetic form factors  $G_E(Q^2)$  and  $G_M(Q^2)$  defined below would be the Fourier transforms of the distribution of charge and magnetization in the nucleon and the rms charge and magnetization radii would be given by their slopes at zero momentum transfer,  $\langle r^2 \rangle_{E,M} = -6G'_{E,M}(0)/G_{E,M}(0)$ . Relativistically, these Sachs form factors may be regarded as three dimensional Fourier transforms of charge and current densities suitably defined in the Breit frame. In addition, Burkardt [1, 2] has shown that the Dirac and Pauli form factors  $F_1(Q^2)$  and  $F_2(Q^2)$  also correspond to two dimensional Fourier transforms of transverse charge and current densities defined in the infinite momentum frame, complementing our knowledge of quark distributions in the infinite momentum frame from deep inelastic scattering. At sufficiently high momentum transfer  $Q^2$ , asymptotic scaling sets in and elastic form factors follow simple counting rules based on the minimum number of gluon exchanges required to divide the momentum transfer equally among all the quarks in the hadron. In the nucleon, at least two gluon exchanges are required so that the electric form factor falls off as  $Q^{-4}$ . The scale determining the onset of asymptotic scaling is of great interest in non-perturbative QCD.

Because of their fundamental physical content, electromagnetic form factors have continued to be studied extensively experimentally throughout the world as technology has improved, but even now, significant questions remain. The most accurately measured form factor is the dominant  $F_1(Q^2)$  form factor for the proton. However, its slope at very low  $Q^2$  is still uncertain. One problem, which has generated considerable theoretical and experimental interest, is that there is a  $7\sigma$  discrepancy between the 2010 CODATA value [3] for the rms charge radius measured using electron-proton elastic scattering and spectroscopy, and the smaller value recently measured using the Lamb shift in muonic hydrogen [4]. Another problem is that phenomenological fits to experimental electron scattering form factors [5, 6] have been inconsistent with analyses based on dispersion theory [7–10]. Interestingly, the charge radius determined using

<sup>\*</sup> Current address: *Institut für Kernphysik, Johannes Gutenberg-Universität Mainz, D-55099 Mainz, Germany*

<sup>†</sup> Current address: *RIKEN BNL Research Center, Brookhaven National Laboratory, Upton, NY 11973, USA*

dispersion theory agrees with the Lamb shift result. Measurements of  $F_2(Q^2)$  using spin polarization [11–15] differ significantly from traditional measurements based on Rosenbluth separation. Although two-photon exchange processes contribute much more strongly to the backward cross section used in Rosenbluth separation than to polarization transfer [6], there are not yet precise theoretical calculations of two photon exchange that resolve the discrepancy. To measure the two photon exchange contribution directly, experiments using  $e^+p$  scattering, for which the relative contribution of the two-photon term changes sign, have been performed by the CLAS experiment at Jefferson Lab Hall B [16, 17], at the VEPP-3 Storage ring in Novosibirsk [18, 19], and by the OLYMPUS experiment at the DORIS storage ring at DESY [20, 21], although none of the three has published final results. Finally, neutron form factors are less accurately determined than proton form factors because of uncertainty in nuclear wave functions for deuterium or  $^3\text{He}$ . Hence, for all these reasons, definitive lattice calculations can play an important role in resolving significant experimental uncertainties.

The Dirac and Pauli form factors,  $F_1^q(Q^2)$  and  $F_2^q(Q^2)$ , parameterize matrix elements of the vector current between proton states:

$$\langle \vec{p}', \lambda' | V_q^\mu | \vec{p}, \lambda \rangle = \bar{u}(\vec{p}', \lambda') \left[ \gamma^\mu F_1^q(Q^2) + \frac{i\sigma^{\mu\nu}(p' - p)_\nu}{2m_N} F_2^q(Q^2) \right] u(p, \lambda), \quad (1)$$

where  $Q^2 = -(p' - p)^2$  and  $V_q^\mu = \bar{q}\gamma^\mu q$ . In comparing with experiment, we also consider form factors of the electromagnetic current  $V_{\text{em}}^\mu = \frac{2}{3}\bar{u}\gamma^\mu u - \frac{1}{3}\bar{d}\gamma^\mu d$  in a proton and in a neutron,  $F_{1,2}^{p,n}(Q^2)$ . Isovector and isoscalar form factors are defined by

$$F_{1,2}^v(Q^2) = F_{1,2}^p(Q^2) - F_{1,2}^n(Q^2) = F_{1,2}^u(Q^2) - F_{1,2}^d(Q^2) \equiv F_{1,2}^{u-d}(Q^2) \quad (2)$$

$$F_{1,2}^s(Q^2) = F_{1,2}^p(Q^2) + F_{1,2}^n(Q^2) = \frac{1}{3}(F_{1,2}^u(Q^2) + F_{1,2}^d(Q^2)) \equiv \frac{1}{3}F_{1,2}^{u+d}(Q^2). \quad (3)$$

The electric and magnetic Sachs form factors  $G_E(Q^2)$  and  $G_M(Q^2)$  are defined by:

$$G_E(Q^2) = F_1(Q^2) - \frac{Q^2}{(2m_N)^2} F_2(Q^2) \quad (4)$$

$$G_M(Q^2) = F_1(Q^2) + F_2(Q^2). \quad (5)$$

Electromagnetic form factors have previously been calculated in lattice QCD using a variety of actions, but so far using pion masses substantially higher than the physical pion mass. Early calculations have been described in review articles [22, 23], including the pioneering calculations of nucleon electric [24] and magnetic [25] form factors using quenched fermions, as well as later quenched calculations [26–32]. Calculations with  $N_f = 2$  flavors have been performed using Wilson [32], clover-improved Wilson [33, 34], domain wall [35], and twisted mass [36, 37] actions.  $N_f = 2 + 1$  calculations have used clover-improved Wilson [38, 39] and domain wall [40–42] actions, and a mixed action with domain wall valence quarks and Asqtad sea quarks [43, 44]. Finally, calculations with  $N_f = 2 + 1 + 1$  flavors have been performed using twisted mass action [45] and a mixed action with clover-improved Wilson valence quarks and HISQ sea quarks [46].

This present work advances the calculation of electromagnetic form factors using lattice QCD in two crucial ways. One essential advance is calculation at the nearly physical pion mass of 149 MeV. Previous calculations referenced above clearly show that for large pion masses, the form factors  $F_1(Q^2)$  and  $F_2(Q^2)$  at low  $Q^2$  lie significantly above the physical values and monotonically decrease toward them as the pion mass is decreased. This behavior is clear physically, because the size of the pion cloud increases strongly as the pion mass decreases so that the rms radius and consequently the slope of the form factor at  $Q^2 = 0$  increase strongly. Quantitatively, the dramatic increase in the isovector Dirac radius as the pion mass decreases arises from the  $\log(m_\pi)$  term in chiral perturbation theory. The second crucial advance is the removal of contamination due to excited states. Having already seen [47] the importance of the removal of excited state contaminants in obtaining agreement with experiment for the radii  $(r_{1,2}^2)^v$ , it is clearly important to do the same for the full  $Q^2$  dependence and we do this using two methods described below. The removal of excited state contaminants in form factors has also been addressed recently [48, 49] for form factors calculated with  $N_f = 2$  Wilson-clover fermions at  $m_\pi \geq 195$  MeV. We find that the combination of calculation at the nearly physical mass of 149 MeV and removal of contamination due to excited states produces excellent agreement with experiment.

The outline of the paper is as follows. Section II presents the lattice methodology, beginning with the description of the clover-improved Wilson action from the Budapest-Marseille-Wuppertal (BMW) collaboration and the ensembles of configurations that are used. Three methods of calculating the relevant matrix elements of the electromagnetic current are then described, the standard ratio method, the summation method, and the generalized pencil-of-function (GPoF) method, from which form factors are extracted by an overdetermined analysis to minimize the statistical

Table I. Gauge configuration ensembles and measurement counts for form factor calculations. The coarse ensembles have gauge coupling  $\beta = 3.31$  and bare strange quark mass  $am_s = -0.04$ , while the fine ensemble has  $\beta = 3.5$  and  $am_s = -0.006$ .

$m_\pi$ [MeV]	$m_N$ [GeV]	$a$ [fm]	$am_{ud}$	$L_s^3 \times L_t$	$m_\pi L_s$	$m_\pi L_t$	$N_{\text{conf}}$	$N_{\text{meas}}$
149(1)	0.929(19)	0.116	-0.09900	$48^3 \times 48$	4.21	4.21	646	7752
202(1)	1.003(22)	0.116	-0.09756	$32^3 \times 48$	3.81	5.71	457	5484
253(1)	1.030(23)	0.116	-0.09530	$32^3 \times 96$	4.78	14.34	202	2424
254(1)	1.051(13)	0.116	-0.09530	$32^3 \times 48$	4.79	7.18	420	5040
254(1)	1.041(15)	0.116	-0.09530	$32^3 \times 24$	4.79	3.59	2074	12444
254(2)	1.072(7)	0.116	-0.09530	$24^3 \times 48$	3.60	7.19	1019	24456
252(2)	1.072(7)	0.116	-0.09530	$24^3 \times 24$	3.56	3.56	3999	23994
303(2)	1.043(51)	0.116	-0.09300	$24^3 \times 48$	4.28	8.56	128	768
317(2)	1.153(20)	0.093	-0.04630	$32^3 \times 64$	4.76	9.52	103	824
356(2)	1.175(18)	0.116	-0.09000	$24^3 \times 48$	5.04	10.08	127	762
351(2)	1.163(13)	0.116	-0.09000	$24^3 \times 24$	4.97	4.97	420	2520

uncertainty. In section III, we present our results for isovector observables. Dirac form factors  $F_1^v(Q^2)$  and Pauli form factors  $F_2^v(Q^2)$  are calculated for ensembles with a range of pion masses and results using the ratio, summation, and GPoF methods are compared. For use in calculating rms radii, dipole fits to these form factors are performed for several ranges of  $Q^2$  and compared to establish insensitivity to the  $Q^2$  range for sufficiently low  $Q^2$ . In one of the highlights of this work, Sachs form factors,  $G_E(Q^2)$  and  $G_M(Q^2)$ , are calculated at the lowest pion mass, 149 MeV, and shown to produce excellent agreement with phenomenological fits to electron scattering data. The Dirac radius,  $(r_1^2)^v$ , Pauli radius,  $(r_2^2)^v$  and anomalous magnetic moment  $\kappa^v$  are calculated for ensembles with a range of pion masses and chirally extrapolated to the physical pion mass. Section IV presents analogous results for isoscalar observables. Finally, we show the proton Sachs form factors in section V and present our conclusions in section VI.

We include three appendices. Appendix A gives details on chiral extrapolation formulae and phenomenological inputs for isovector observables. Appendix B includes additional plots comparing, for observables where this was omitted in the main text, results computed on each ensemble using the ratio, summation, and GPoF methods; this is intended to be useful for others performing similar lattice QCD calculations. Finally, Appendix C has tables listing form factors for four ensembles.

## II. LATTICE METHODOLOGY

### A. Lattice action and gauge ensembles

We perform lattice QCD calculations using a tree-level Symanzik-improved gauge action and 2+1 flavors of tree-level improved Wilson-clover quarks, which couple to the gauge links via two levels of HEX smearing as motivated by Ref. [50]. For a detailed description of the action and smearing procedure we refer the reader to [51]. The  $s$  quarks are tuned to have a mass close to physical, and the light quark mass (with  $m_u = m_d$ ) is varied, yielding pion masses between 149 and 356 MeV. The algorithms used to generate the gauge field ensembles are described in [51].

In Tab. I we list the gauge ensembles analyzed in this paper. In Fig. 1 we show  $(m_\pi, L)$  values in comparison to other lattice calculations of nucleon structure [34, 37–42, 44–46, 49]. We check the volume dependence of our results at  $m_\pi = 254$  MeV by varying the physical volume from  $(3.7 \text{ fm})^3$  to  $(2.8 \text{ fm})^3$ . We perform all calculations with  $a = 0.116$  fm except one with  $m_\pi = 317$  MeV and  $a = 0.093$  fm to check for discretization effects. In addition, at  $m_\pi \approx 250$  and  $\approx 350$  MeV we vary the time extent of the lattices between 2.8 fm and 11.1 fm to check whether thermal states [52] have any effect on the nucleon structure observables that we calculate.

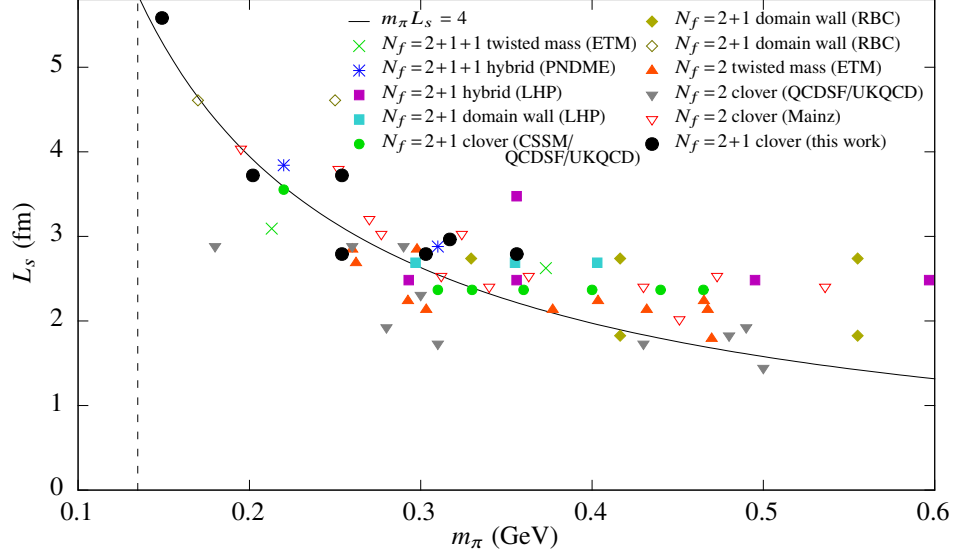


Figure 1. Summary of pion masses and volumes in existing lattice calculations of nucleon structure. Open symbols are used to indicate cases where results were described by the authors as “preliminary”.

## B. Computation of matrix elements

In order to measure nucleon matrix elements in lattice QCD, we compute nucleon two-point and three-point functions,

$$C_{2\text{pt}}(\vec{p}, t) = \sum_{\vec{x}} e^{-i\vec{p} \cdot \vec{x}} \text{Tr}[\Gamma_{\text{pol}} \langle N(\vec{x}, t) \bar{N}(\vec{0}, 0) \rangle] \quad (6)$$

$$C_{3\text{pt}}^{V_q^\mu}(\vec{p}, \vec{p}', \tau, T) = \sum_{\vec{x}, \vec{y}} e^{-i\vec{p}' \cdot \vec{x}} e^{i(\vec{p}' - \vec{p}) \cdot \vec{y}} \text{Tr}[\Gamma_{\text{pol}} \langle N(\vec{x}, T) V_q^\mu(\vec{y}, \tau) \bar{N}(\vec{0}, 0) \rangle], \quad (7)$$

where  $N = \epsilon^{abc}(\tilde{u}_a^T C \gamma_5 \frac{1+\gamma_4}{2} \tilde{d}_b) \tilde{u}_c$  is a proton interpolating operator constructed using smeared quark fields,  $V_q^\mu = \bar{q} \gamma^\mu q$  is the site-local vector current, and  $\Gamma_{\text{pol}} = \frac{1+\gamma_4}{2} \frac{1-i\gamma_3\gamma_5}{2}$  is a spin and parity projection matrix. For smearing, we use approximately-Gaussian Wuppertal smearing [53] with the same double-HEX-smeared links as used for the fermion action. We compute  $C_{3\text{pt}}$  with both  $\vec{p}' = \vec{0}$  and  $\vec{p}' = \frac{2\pi}{L_s}(-1, 0, 0)$ , and for quark flavors  $q \in \{u, d\}$ . The three-point correlators have contributions from both connected and disconnected quark contractions, but we compute only the connected part. Omitting the disconnected part (where the vector current is attached to a quark loop) introduces an uncontrolled systematic error except when taking the  $u - d$  (isovector) flavor combination, where the disconnected contributions cancel out. The magnitude of disconnected contributions is discussed in the conclusions (Sec. VI).

On a lattice with finite time extent  $L_t$ , the transfer matrix formalism yields

$$C_{2\text{pt}}(\vec{p}, t) = \sum_{n, m} e^{-E_m L_t} e^{-(E_n - E_m)t} \sum_{\alpha, \beta} (\Gamma_{\text{pol}})_{\alpha\beta} \sum_{\vec{x}} e^{-i\vec{p} \cdot \vec{x}} \langle m | N_\beta(\vec{x}) | n \rangle \langle n | \bar{N}_\alpha(\vec{0}) | m \rangle \quad (8)$$

$$C_{3\text{pt}}^{V_q^\mu}(\vec{p}, \vec{p}', \tau, T) = \sum_{n, n', m} e^{-E_m L_t} e^{-(E_n - E_m)\tau} e^{-(E_{n'} - E_m)(T - \tau)} \sum_{\alpha, \beta} (\Gamma_{\text{pol}})_{\alpha\beta} \times \sum_{\vec{x}, \vec{y}} e^{-i\vec{p}' \cdot \vec{x}} e^{i(\vec{p}' - \vec{p}) \cdot \vec{y}} \langle m | N_\beta(\vec{x}) | n' \rangle \langle n' | V_q^\mu(\vec{y}) | n \rangle \langle n | \bar{N}_\alpha(\vec{0}) | m \rangle. \quad (9)$$

Thermal contamination is eliminated in the large  $L_t$  (zero-temperature) limit, in which state  $m$  is the vacuum, and states  $n$  and  $n'$  are restricted to having the quantum numbers of a proton with momentum  $\vec{p}$  and  $\vec{p}'$ , respectively. Unwanted contributions from excited states can be eliminated by then taking  $\tau$  and  $T - \tau$  to be large.

In order to compute  $C_{3\text{pt}}$ , we use sequential propagators through the sink [24]. This has the advantage of allowing for any operator to be measured at any time using a fixed set of quark propagators, but new backward propagators must be computed for each source-sink separation  $T$ . Increasing  $T$  suppresses excited-state contamination, but it

also increases the noise; the signal-to-noise ratio is expected to decay asymptotically as  $e^{-(m_N - \frac{3}{2}m_\pi)T}$  [54]. Past calculations have often used a single source-sink separation, which only allows for a limited ability to identify and remove excited state contamination. In particular, when computing forward matrix elements, there is no way of distinguishing contributions from excited states with  $n' = n$  from the ground state contribution, when using  $C_{3\text{pt}}$  with a single  $T$ . Therefore, in this work, we perform measurements using three source-sink separations on all ensembles:  $T/a \in \{8, 10, 12\}$  for the coarse lattices and  $T/a \in \{10, 13, 16\}$  for the fine lattice.

### 1. Ratio method

We label proton states as  $|\vec{p}, \lambda\rangle$  and use the relativistic normalization,  $\langle \vec{p}', \lambda' | \vec{p}, \lambda \rangle = 2EL_s^3 \delta_{\vec{p}', \vec{p}} \delta_{\lambda', \lambda}$ . Parameterizing the overlap of our interpolating operator with the ground-state proton as  $\langle \Omega | N_\alpha(\vec{x}) | \vec{p}, \lambda \rangle = \sqrt{Z(\vec{p})} u_\alpha(\vec{p}, \lambda) e^{i\vec{p} \cdot \vec{x}}$ , at zero temperature we obtain

$$C_{2\text{pt}}(\vec{p}, t) = \frac{Z(\vec{p})e^{-E(\vec{p})t}}{2E(\vec{p})} \text{Tr}[\Gamma_{\text{pol}}(i\not{p} + m_N)] + O(e^{-\Delta E_{10}(\vec{p})t}) \quad (10)$$

$$C_{3\text{pt}}^{V_q^\mu}(\vec{p}, \vec{p}', \tau, T) = \frac{\sqrt{Z(\vec{p})Z(\vec{p}')e^{-E(\vec{p})\tau - E(\vec{p}')(T-\tau)}}}{4E(\vec{p}')E(\vec{p})} \sum_{\lambda, \lambda'} \bar{u}(\vec{p}, \lambda) \Gamma_{\text{pol}} u(\vec{p}', \lambda') \langle p', \lambda' | V_q^\mu | p, \lambda \rangle \quad (11)$$

$$+ O(e^{-\Delta E_{10}(\vec{p})\tau}) + O(e^{-\Delta E_{10}(\vec{p}')(T-\tau)}),$$

where  $\Delta E_{10}(\vec{p})$  is the energy gap between the ground and lowest excited state with momentum  $\vec{p}$ . To cancel the overlap factors and the dependence on Euclidean time, we compute the *ratios*,

$$R_q^\mu(\tau, T) = \frac{C_{3\text{pt}}^{V_q^\mu}(\vec{p}, \vec{p}', \tau, T)}{\sqrt{C_{2\text{pt}}(\vec{p}, T)C_{2\text{pt}}(\vec{p}', T)}} \sqrt{\frac{C_{2\text{pt}}(\vec{p}, T-\tau)C_{2\text{pt}}(\vec{p}', \tau)}{C_{2\text{pt}}(\vec{p}', T-\tau)C_{2\text{pt}}(\vec{p}, \tau)}} \quad (12)$$

$$= \frac{\sum_{\lambda, \lambda'} \bar{u}(\vec{p}, \lambda) \Gamma_{\text{pol}} u(\vec{p}', \lambda') \langle p', \lambda' | V_q^\mu | p, \lambda \rangle}{\sqrt{2E(\vec{p})(E(\vec{p}) + m_N) \cdot 2E(\vec{p}')(E(\vec{p}') + m_N)}} + O(e^{-\Delta E_{10}(\vec{p})\tau}) + O(e^{-\Delta E_{10}(\vec{p}')(T-\tau)}).$$

As a function of  $\tau \in [0, T]$  with fixed  $T$ , the ratios produce a plateau with “tails” at both ends caused by excited states. In practice, for each fixed  $T$ , we average over the central two or three points near  $\tau = T/2$ , which allows for matrix elements to be computed with errors that decay asymptotically as  $e^{-\Delta E_{\min}T/2}$ , where  $\Delta E_{\min} = \min\{\Delta E_{10}(\vec{p}), \Delta E_{10}(\vec{p}')\}$ .

### 2. Summation method

Improved asymptotic behavior of excited-state contributions can be achieved by using the summation method [55, 56]. Taking the sums of ratios yields

$$S(T) \equiv \sum_{\tau=\tau_0}^{T-\tau_0} R(\tau, T) = c + TM + O(Te^{-\Delta E_{\min}T}), \quad (13)$$

where  $c$  is independent of  $T$ , and  $M$  contains the desired ground-state matrix element. (We choose  $\tau_0 = 1$  and thus omit the first and last points of each plateau.) Thus finite differences,  $(\delta T)^{-1}(S(T+\delta T) - S(T))$ , yield the ground-state matrix element with excited-state contamination that asymptotically decays as  $Te^{-\Delta E_{\min}T}$ . In particular, transitions between the ground and lowest excited state, which were the dominant excited-state contribution for the ratio method at large time separations, are highly suppressed, now decaying as  $e^{-\Delta E_{\min}T}$ .

With our three source-sink separations, we can compute this finite difference at two values of  $T$ , however the result at the larger value of  $T$  tends to have very large statistical uncertainties. Instead of using a finite difference, we fit a line  $a + bT$  to our three  $S(T)$  points, and take the slope  $b$  as the extracted matrix element. The result is mostly determined from the lower two source-sink separations, as their sums have smaller errors, but choosing this fit over a finite difference allows the larger source-sink separation to also have some influence.

### 3. Generalized pencil-of-function method

By using  $n$  interpolating operators, the variational method [57, 58] allows for asymptotically removing the unwanted contributions from the first  $n - 1$  excited states. We are able to make use of the variational method via the generalized pencil-of-function (GPoF) method [59], which is based on the recognition that if  $N(t)$  and  $\bar{N}(t)$  are our interpolating operators for annihilating and creating the nucleon, then the time-displaced operators

$$N^\delta(t) \equiv e^{H\delta} N(t) e^{-H\delta} = N(t + \delta) \quad (14)$$

$$\bar{N}^\delta(t) \equiv e^{-H\delta} \bar{N}(t) e^{H\delta} = \bar{N}(t - \delta) \quad (15)$$

are linearly independent interpolating operators for the nucleon. This enables us to construct a matrix of two-point functions,

$$\mathbf{C}_{2\text{pt}}(t) = \begin{pmatrix} \langle N(t) \bar{N}(0) \rangle & \langle N^\delta(t) \bar{N}(0) \rangle \\ \langle N(t) \bar{N}^\delta(0) \rangle & \langle N^\delta(t) \bar{N}^\delta(0) \rangle \end{pmatrix} = \begin{pmatrix} C_{2\text{pt}}(t) & C_{2\text{pt}}(t + \delta) \\ C_{2\text{pt}}(t + \delta) & C_{2\text{pt}}(t + 2\delta) \end{pmatrix}, \quad (16)$$

using our ordinary two-point function  $C_{2\text{pt}}(t)$ . By solving the generalized eigenvalue problem,

$$\mathbf{C}_{2\text{pt}}(t) \mathbf{v}(t_0, t) = \lambda(t_0, t) \mathbf{C}_{2\text{pt}}(t_0) \mathbf{v}(t_0, t) \quad (17)$$

we can find eigenvectors  $\mathbf{v}(t_0, t)$  that asymptotically give linear combinations of  $N$  and  $N^\delta$  which have zero overlap with the first excited state. Then using also the matrix of three-point functions,

$$\mathbf{C}_{3\text{pt}}(\tau, T) = \begin{pmatrix} \langle N(T) \mathcal{O}(\tau) \bar{N}(0) \rangle & \langle N^\delta(T) \mathcal{O}(\tau) \bar{N}(0) \rangle \\ \langle N(T) \mathcal{O}(\tau) \bar{N}^\delta(0) \rangle & \langle N^\delta(T) \mathcal{O}(\tau) \bar{N}^\delta(0) \rangle \end{pmatrix} = \begin{pmatrix} C_{3\text{pt}}(\tau, T) & C_{3\text{pt}}(\tau, T + \delta) \\ C_{3\text{pt}}(\tau + \delta, T + \delta) & C_{3\text{pt}}(\tau + \delta, T + 2\delta) \end{pmatrix}, \quad (18)$$

we compute two-point and three-point functions using a particular linear combination:

$$C_{2\text{pt}}^{\text{GPoF}}(t) = \mathbf{v}^\dagger \mathbf{C}_{2\text{pt}}(t) \mathbf{v} \quad C_{3\text{pt}}^{\text{GPoF}}(\tau, T) = \mathbf{v}^\dagger \mathbf{C}_{3\text{pt}}(\tau, T) \mathbf{v}, \quad (19)$$

and then proceed with the usual ratio-plateau analysis. Note that this requires computing three-point functions at three equally spaced source-sink separations, which is precisely what we have, and thus we can only compute  $C_{3\text{pt}}^{\text{GPoF}}(\tau, T)$  at our shortest source-sink separation  $T$ .

Consider, for example, a  $2 \times 2$  GPoF analysis applied to a system with exactly two states,  $E_0$  and  $E_1$ . It is trivial to show that the eigenstates  $\lambda(t_0, t)$  in Eq. (17) are equal to  $e^{-E_{0,1}(t-t_0)}$  and the eigenvectors are  $\mathbf{v}_{0,1}^T = (-e^{-E_{1,0}\delta}, 1)$ . Substituting the ground state eigenvector  $\mathbf{v}_0$  into Eq. (19), we obtain

$$\begin{aligned} C_{2\text{pt}}^{\text{GPoF}}(t) &= C_{2\text{pt}}(t + 2\delta) - 2e^{-E_1\delta} C_{2\text{pt}}(t + \delta) + e^{-2E_1\delta} C_{2\text{pt}}(t), \\ C_{3\text{pt}}^{\text{GPoF}}(\tau, T) &= C_{3\text{pt}}(\tau + \delta, T + 2\delta) - e^{-E_1\delta} (C_{3\text{pt}}(\tau, T + \delta) + C_{3\text{pt}}(\tau + \delta, T + \delta)) + e^{-2E_1\delta} C_{3\text{pt}}(\tau, T), \end{aligned} \quad (20)$$

indicating that, if computed using the GPoF method, the ground state matrix elements and their uncertainties will be mostly determined by the values of correlators with the largest separation  $T$ .

In practice, for each class of lattice momenta  $\vec{p}$  equivalent under the group of lattice rotations and reflections, we average the two-point correlators  $C_{2\text{pt}}(t, \vec{p})$  and then use the GPoF method and solve the generalized eigenvalue problem. This produces a different linear combination of the original and the time-displaced nucleon operator for each class of equivalent lattice momenta. It has been shown [58] that by appropriately increasing  $t_0$  and  $t$  as  $\tau$  and  $T - \tau$  are increased, the contributions from the lowest-lying excited state can be completely removed asymptotically; however, in this work, we find the eigenvector using the fixed values  $t_0/a = 1$  and  $t/a = 2$ . As shown in Fig. 2, this is sufficient to remove the effect of excited-state contamination in  $C_{2\text{pt}}^{\text{GPoF}}$  at the present level of statistics.

### 4. Comparison of methods for computing matrix elements

Given our level of statistical error and that we have only three source-sink separations, there are trade-offs between the three methods for computing matrix elements:

- Although the ratio method has the worst asymptotic behavior, we are able to compute one result for each source-sink separation, which gives an indication of the approach to the ground-state matrix element.

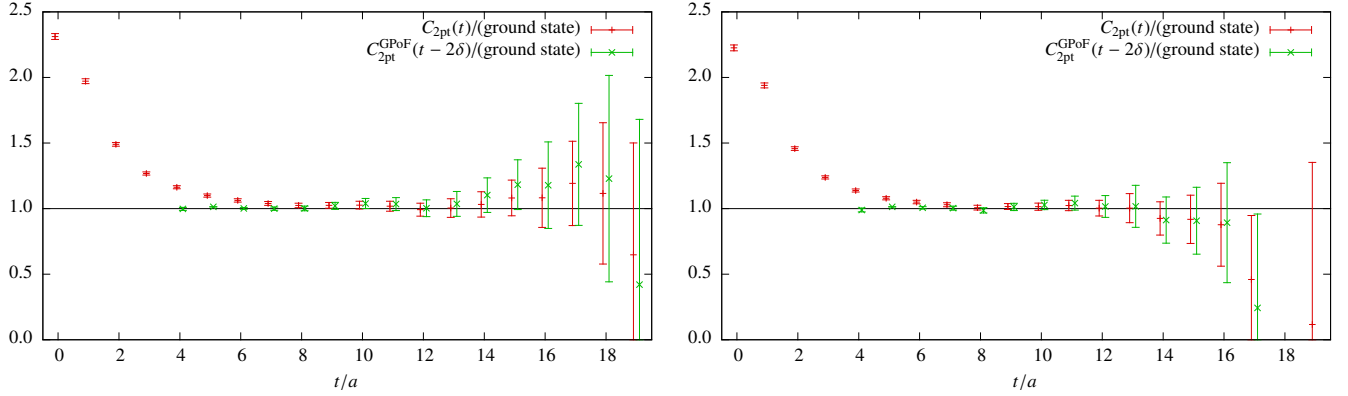


Figure 2. Two-point correlators  $C_{2pt}(t, \vec{p})$  and  $C_{2pt}^{\text{GPOF}}(t, \vec{p})$  for the 149 MeV ensemble, divided by their ground-state contributions, as determined from a two-state fit to the former with  $t/a \in [3, 14]$  and a one-state fit to the latter with  $t/a \in [2, 12]$ . The left plot has  $\vec{p} = \vec{0}$ , and the right plot is averaged over  $a\vec{p}$  equivalent to  $\frac{2\pi}{48}(2, 1, 1)$ , which is the largest used for computing matrix elements on this ensemble. The GPOF correlators are shifted to show that at large times their dominant contribution is from the time-displaced nucleon interpolating operator.

- The summation method asymptotically suppresses excited-state contributions without requiring knowledge about any particular state. In particular, this method is most effective at suppressing the contributions from transition matrix-elements between the ground state and an excited state.
- If excited-state contributions to two-point and three-point functions come mostly from a single state, then (given sufficient statistics) the GPOF method is effective at removing them. In particular, this removal will include contributions to the two-point function and both ground-to-excited and excited-to-excited matrix elements in the three-point function.

The case of contamination from transition matrix elements is, in particular, one where the GPOF method could in practice be not very successful at removing the effect of excited states. Consider an excited state with a small amplitude relative to the ground state. That is,  $r \equiv \sqrt{Z'/Z}$  is small, where  $Z$  is defined as above and  $Z'$  is defined analogously for the excited state. Then the contribution from this state to the two-point function would be suppressed as  $r^2$ , such that it could disappear into statistical noise. However, its contribution to three-point functions via transitions to the ground state would only be suppressed by the factor  $r$ . Since the GPOF method relies on the two-point function for optimizing its effective interpolating operator, it could fail to remove such excited-state contributions.

For a concise presentation, we select a single method for our primary results, namely the summation method, as it is effective at suppressing contributions from all excited states, is fairly simple, and has been used successfully in computing the nucleon axial charge [49, 60]. The GPOF method has not seen widespread use, and our set of results using it should be considered an exploratory study. We will see (in the main text and in Appendix B) that, with the present level of statistics, results using the ratio (with the largest source-sink separation), summation, and GPOF methods are consistent with one another and therefore this choice does not have a significant effect on the results.

The two main methods not considered here are multi-state fitting and broader application of the variational method with different interpolating operators (beyond just the time-displacements used by GPOF). In recent years, the former has been applied to nucleon matrix elements in Refs. [46, 61–63], typically with the assumption that only two states contribute in the range of probed time separations. The latter has been used extensively in spectroscopy calculations together with a large number of interpolating operators; see, e.g., Ref. [64] for an application to excited baryons. It has also seen some use for nucleon matrix elements, such as the calculations in Refs. [65, 66]. These used sequential propagators from a fixed current rather than a fixed sink as was used in this work; this reduces the cost of including several interpolating operators, with the drawback of requiring additional propagators for each current insertion.

### C. Extraction of form factors

The renormalized  $O(a)$ -improved vector current is given by [67]

$$(V_q^\mu)_R = Z_V(1 + b a m_q)(V_q^\mu + c a \partial^\nu T_q^{\mu\nu}), \quad (21)$$

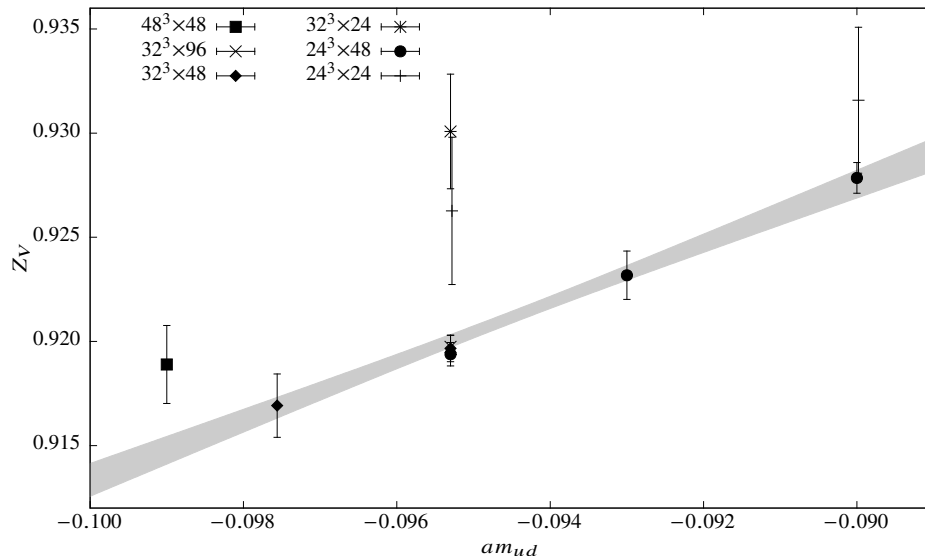


Figure 3. Vector current renormalization factor  $Z_V$  versus bare quark mass, for the coarse ensembles. The band is from a fit assuming a linear relationship.

where  $T_q^{\mu\nu} = i\bar{q}\sigma^{\mu\nu}q$ . For tree-level improvement, as used in the lattice action,  $b = 1$  and  $c = 0$ . We keep the latter and use only the site-local vector current, but rather than controlling the quark-mass dependence via two parameters  $(Z_V, b)$ , we instead compute a separate  $Z_V$  renormalization factor on each ensemble.

We do this by measuring the time-component of the vector current at  $\vec{p}' - \vec{p} = 0$ , which is (up to renormalization and lattice artifacts) the quark number, a conserved charge. Specifically, we take the  $u - d$  flavor combination and, on each ensemble, impose that it equals 1 for the proton in order to obtain  $Z_V$ . This should be unaffected by excited states in the normal sense; any dependence on time separations should only occur as a result of lattice artifacts or thermal effects. We observe no statistically significant dependence on source-sink separation in our data, and compute  $Z_V$  on each ensemble using the ratio-plateau method with the shortest source-sink separation. For the coarse ensembles, this is shown in Fig. 3. A linear fit has slope  $b = 1.42(13)$ , which is somewhat larger than the tree-level value. We note that the ensembles with small values of  $m_\pi L_t$  tend to have values of  $Z_V$  that lie somewhat above the fit, suggesting the presence of some thermal contamination; this shows up for  $Z_V$  in particular because other sources of uncertainty (including statistical) are smaller than in other observables. As the effect is at the percent level, it is negligible compared to the statistical uncertainty that we later obtain for electromagnetic form factors.

We do notice another clear apparent thermal effect: the statistical uncertainty depends strongly on the time extent. Despite other ensembles having many more measurements, the  $32^3 \times 96$  ensemble has the smallest uncertainty for  $Z_V$ . In addition, the three  $L_t = 24a$  ensembles have the largest uncertainties for  $Z_V$ , and the uncertainties grow more rapidly with the source-sink separation on the ensembles with shorter time extent (not shown in Fig. 3). The more-rapid onset of noise, arising from the influence of thermal states, has been previously examined for the case of (multi-)baryon two-point correlators in Ref. [52].

To compute form factors: for each value of  $Q^2$ , we parameterize the corresponding set of matrix elements of the vector current by  $F_1(Q^2)$  and  $F_2(Q^2)$ , and perform a linear fit to solve the resulting overdetermined system of equations [68], after first combining equivalent matrix elements to improve the condition number [40]. This approach makes use of all available matrix elements in order to minimize the statistical uncertainty in the resulting form factors. On our ensembles, the largest source momentum that we use is  $\vec{p} = \frac{2\pi}{L_s}(1, 1, 1)$ , except for the  $m_\pi = 149$  MeV ensemble, where we use source momenta as large as  $\vec{p} = \frac{2\pi}{L_s}(1, 1, 2)$  to compensate for the larger volume.

### III. ISOVECTOR FORM FACTORS

Isvector lattice observables are particularly interesting because they have no disconnected quark contractions and thus may be compared directly to differences between proton and neutron experimental results.



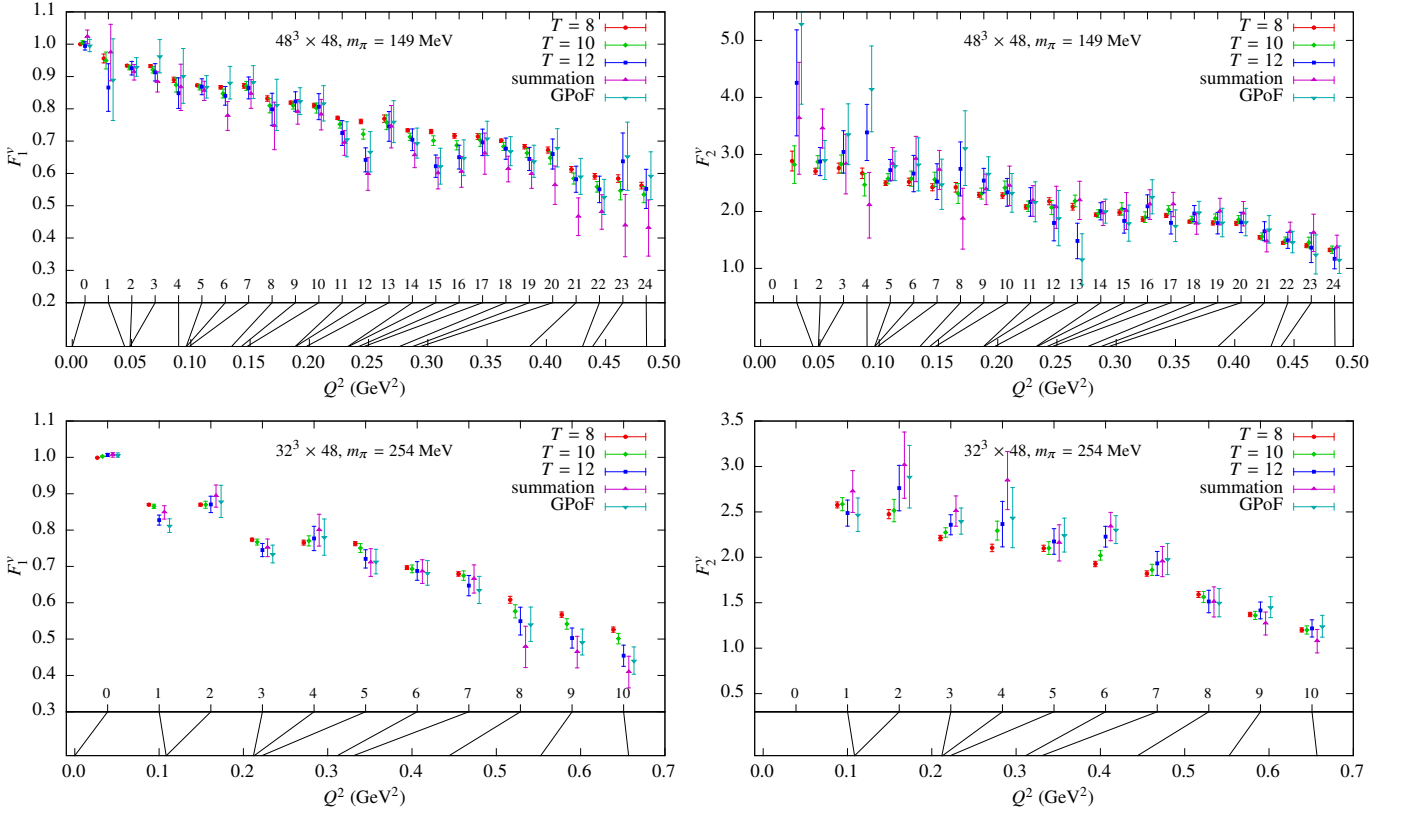


Figure 4. Comparison of different methods to extract the ground state isovector form factors  $F_1^v(Q^2)$  and  $F_2^v(Q^2)$ . The upper plots show the  $m_\pi = 149$  MeV ensemble and the lower plots show the  $m_\pi = 254$  MeV,  $32^3 \times 48$  ensemble.

### A. Form factors

We compute isovector Dirac and Pauli form factors using the different methods discussed in Sec. II B, and results are shown for two ensembles in Fig. 4. A clear trend when going from the lowest to the middle source-sink separation is seen for the  $m_\pi = 149$  MeV ensemble, where  $F_1^v$  tends to decrease and  $F_2^v$  tends to increase. The  $m_\pi = 254$  MeV ensemble shows similar behavior, although not as strongly. As shown in Appendix B, this trend is even less-clear on other ensembles. The GPoF and summation results have similar statistical uncertainties, which are slightly larger than those of the ratio-plateau method with the largest source-sink separation. They are in reasonable agreement, except for the  $m_\pi = 149$  MeV ensemble, where the summation values for  $F_1^v$  consistently lie below the corresponding GPoF values; this suggests that excited-state effects are not fully under control on this ensemble.

In general, the GPoF values tend to stay close to the ratio-method values with the largest source-sink separation, whereas the summation values tend to appear like an “extrapolation” from the trend set by the lowest two source-sink separations; this is consistent with expectations from Sec. II B. This tendency can be seen most clearly when there is a separation between the summation and GPoF values, such as for momentum #23 for  $F_1^v$  on the  $m_\pi = 149$  MeV ensemble.

#### 1. Isovector Dirac form factor $F_1^v(Q^2)$

We perform two-parameter fits of a dipole form,

$$F(Q^2) = \frac{F(0)}{\left(1 + \frac{Q^2}{m_D^2}\right)^2}, \quad (22)$$

in the range  $0 \leq Q^2 < 0.5$  GeV<sup>2</sup>, to  $F_1^v(Q^2)$  for all of our ensembles. This produces good fits, except on some ensembles when using the shortest source-sink separation, where the data have smaller statistical uncertainties. On

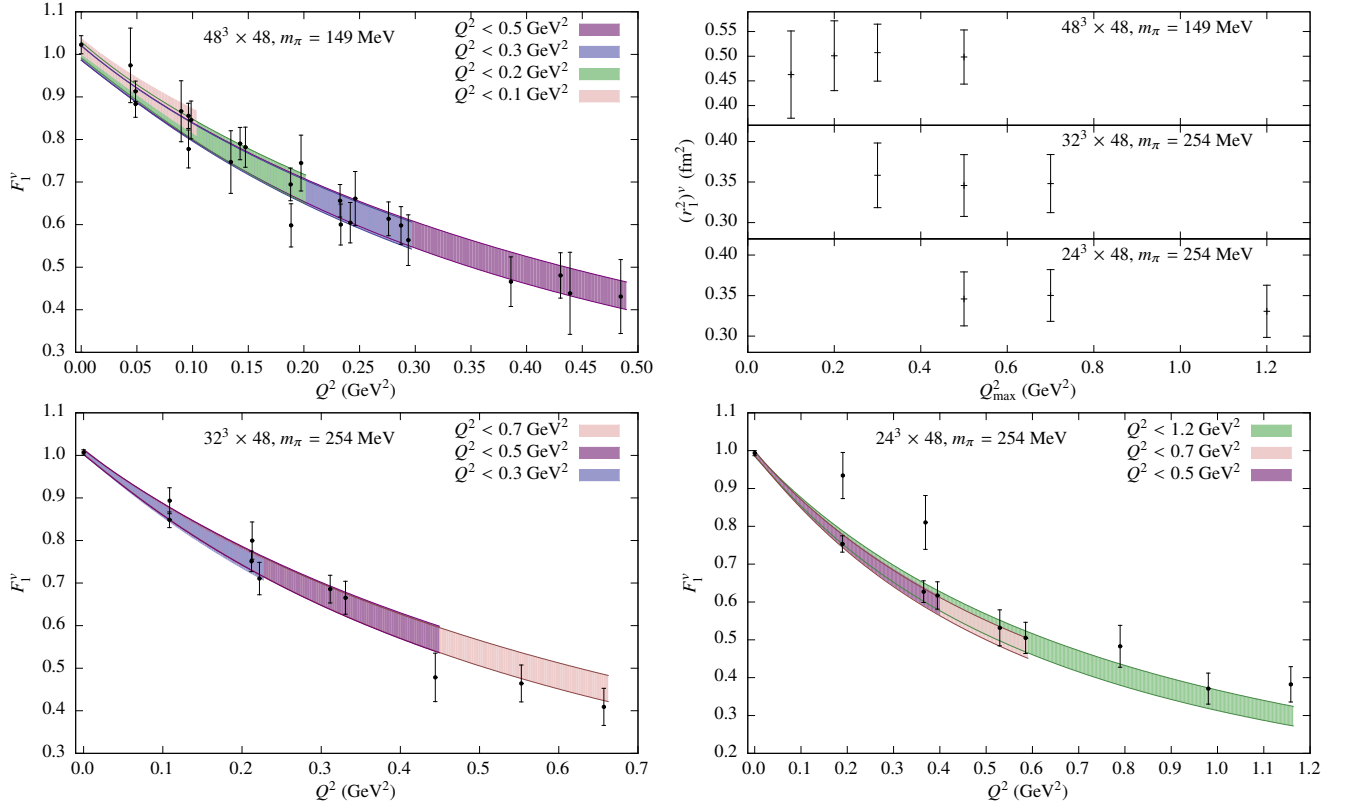


Figure 5. Dipole fits to  $F_1^v(Q^2)$  with varying  $Q_{\max}^2$ . The upper-right plot shows the dependence on  $Q_{\max}^2$  of the isovector Dirac radius derived from the fits.

the  $m_\pi = 149$  MeV ensemble, these data suffer from excited-state contamination, and the fit has  $\chi^2 = 43(13)$  for 23 degrees of freedom. Because the data at larger source-sink separations have larger uncertainties, it is unclear whether this amount of deviation from a dipole form persists when excited-state effects are reduced. The  $24^3 \times 48$  and  $24^3 \times 24$  ensembles at  $m_\pi \approx 250$  MeV also suffer from poor fit quality; this is caused by two momenta that have higher values of  $F_1^v$  than other nearby momenta (visible in Fig. 5; specifically, these are momenta #2 and #4 in Fig. 19). This appears to be a fluctuation, as such a large difference between nearby momenta is not seen on other ensembles.

To study the dependence on the fit form, we perform dipole fits for  $0 \leq Q^2 < Q_{\max}^2$  with varying  $Q_{\max}^2$ , to the summation data on three ensembles; these are shown in Fig. 5. In all three cases, the fit parameters vary with  $Q_{\max}^2$  by less than the statistical uncertainty, with the largest variation occurring on the 149 MeV ensemble, where  $(r_1^2)^v \equiv \frac{12}{m_\pi^2}$  varies between  $0.463(88)$  fm<sup>2</sup> and  $0.507(58)$  fm<sup>2</sup>, and our choice of  $Q_{\max}^2 = 0.5$  GeV<sup>2</sup> yields  $(r_1^2)^v = 0.498(55)$  fm<sup>2</sup>. Therefore we conclude that errors caused by fitting are smaller than the statistical uncertainty.

## 2. Isovector Pauli form factor $F_2^v(Q^2)$

For the isovector Pauli form factor, we again perform two-parameter dipole fits [Eq. (22)] in the range  $0 < Q^2 < 0.5$  GeV<sup>2</sup>; the main difference is that, because of the kinematic factor in Eq. (1), we have no measurement of  $F_2$  at  $Q^2 = 0$ . Therefore, understanding behavior near zero momentum transfer requires an extrapolation below the smallest accessible  $Q_{\min}^2 \sim (\frac{2\pi}{L_s})^2$ , and this extrapolation is more difficult on ensembles with smaller volumes. The quality of fits is generally reasonable, particularly when not using the shortest source-sink separation, which has the most precise data. The most-consistently bad fits are on the  $32^3 \times 48$ ,  $m_\pi = 254$  MeV ensemble, where  $\chi^2$  varies between 11 and 15, depending on how the matrix elements are computed, for fits with 6 degrees of freedom.

We again study dependence on the fit form by varying the maximum momentum transfer included in the fit,  $Q_{\max}^2$ , on three ensembles, using form factors computed using the summation method; these are shown in Fig. 6. Because of the need to extrapolate to  $Q^2 = 0$ , the fit parameters have a greater variation with  $Q_{\max}^2$  than occurred for the Dirac form factor; although on the two shown  $m_\pi = 254$  MeV ensembles, this variation is roughly within the statistical uncertainty of the fit done with our choice of  $Q_{\max}^2 = 0.5$  GeV<sup>2</sup>. On the 149 MeV ensemble, this also holds true for

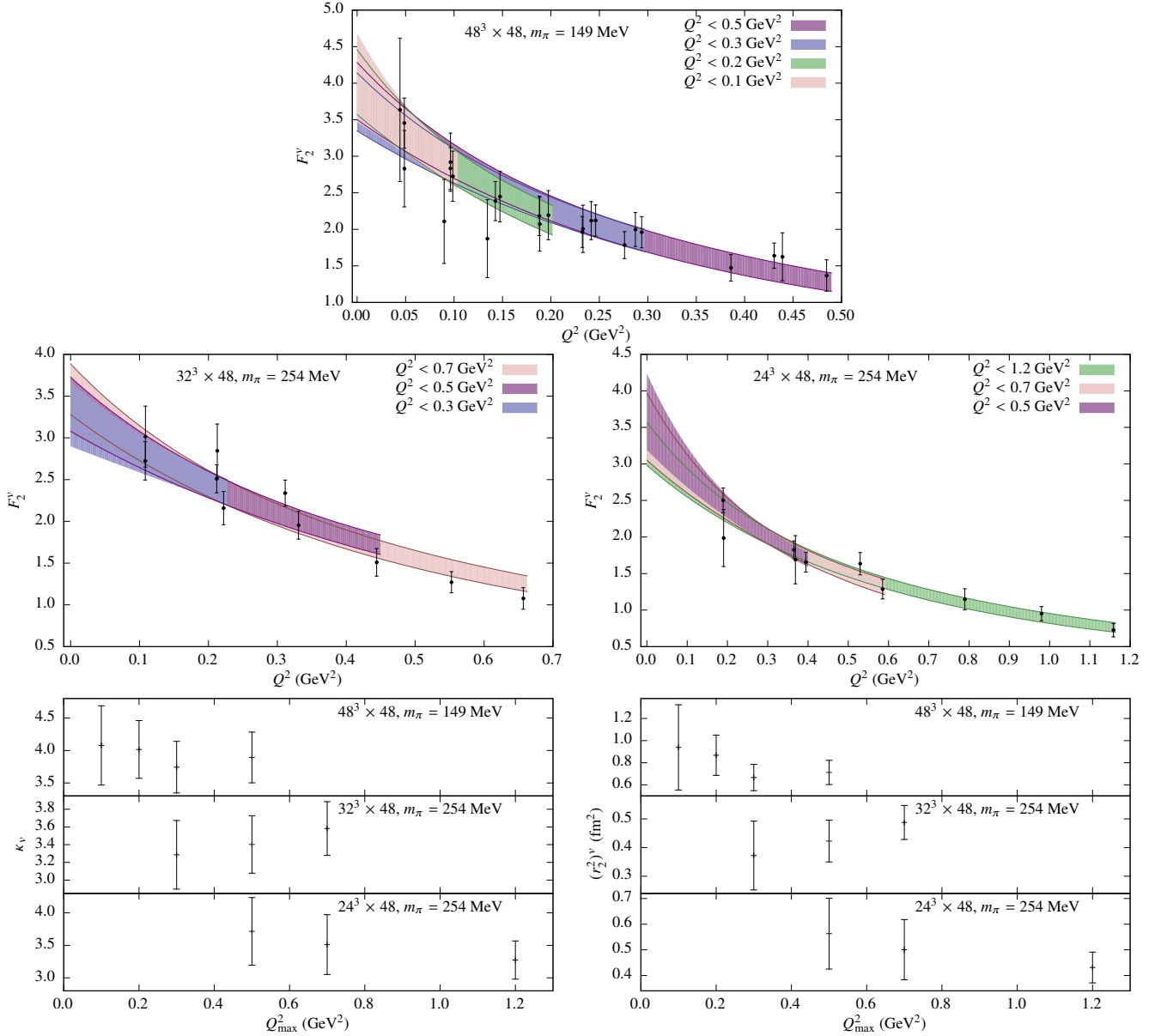


Figure 6. Dipole fits to  $F_2^v(Q^2)$  with varying  $Q_{\max}^2$ . The last two plots show the dependence on  $Q_{\max}^2$  of the fit parameters.

$F_2^v(0)$ , which varies between 3.74(40) and 4.08(61), and our chosen fit yields  $F_2^v(0) = 3.89(39)$ ; however,  $(r_2^2)^v \equiv \frac{12}{m_D^2}$  varies between 0.67(12) fm<sup>2</sup> and 0.94(38) fm<sup>2</sup>, and our chosen fit yields  $(r_2^2)^v = 0.71(11)$  fm<sup>2</sup>. Since the statistical uncertainty increases significantly at small  $Q_{\max}^2$  and the results remain consistent with our choice, we conclude that systematic errors due to fitting are not large.

### 3. Isovector Sachs form factors

To avoid any model-dependence from fitting curves, we first compare the lattice form factors themselves with experiment. In particular, we use the experimentally-preferred electric and magnetic form factors,  $G_E$  and  $G_M$ , and make use of the phenomenological parameterization of experimental data in Ref. [69], for which correlations between fit parameters have been made available, allowing for the curves to be plotted with error bands. These are compared with our summation data from the  $m_\pi = 149$  MeV ensemble in Fig. 7. Both of these form factors agree well with experiment; a chi-squared comparison yields  $p = 0.64$  for  $G_E$  and  $p = 0.81$  for  $G_M$ , a feat that only occurs when both

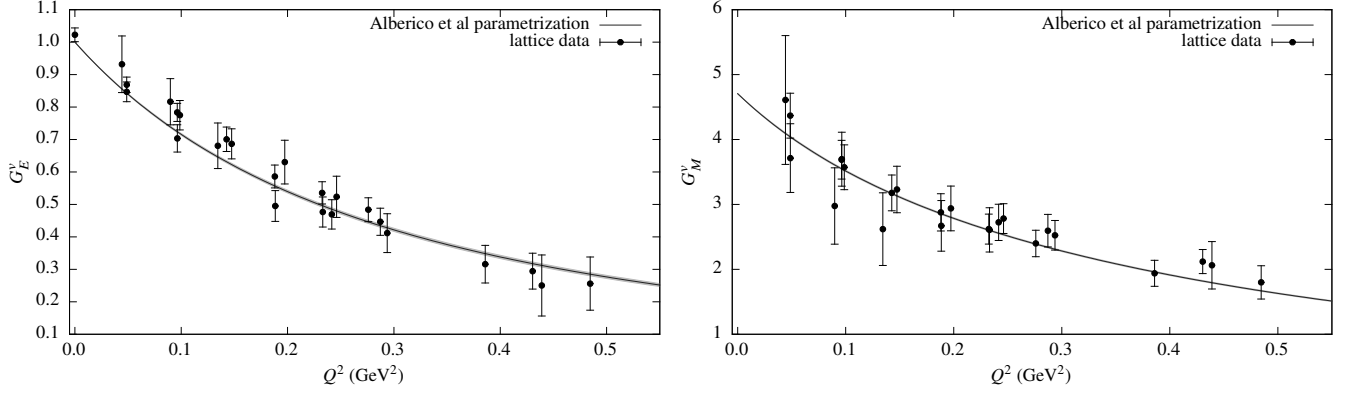


Figure 7. Isovector electric and magnetic form factors. Each plot contains the curve with error band from the fit to experiment in Ref. [69] and the summation data from the  $m_\pi = 149$  MeV ensemble.

the pion mass is near-physical and excited-state contaminations are reasonably controlled. Using the ratio method with the largest source-sink separation or the GPoF method also produces reasonable agreement, with  $p > 0.2$  in all cases.

### B. Isovector Radii and magnetic moment

The isovector Dirac and Pauli radii,  $(r_{1,2}^2)^v$ , and the isovector anomalous magnetic moment,  $\kappa^v$ , are defined from the behavior of  $F_{1,2}^v(Q^2)$  near  $Q^2 = 0$ :

$$F_1^v(Q^2) = 1 - \frac{1}{6}(r_1^2)^v Q^2 + O(Q^4) \quad (23)$$

$$F_2^v(Q^2) = \kappa^v \left( 1 - \frac{1}{6}(r_2^2)^v Q^2 + O(Q^4) \right). \quad (24)$$

On each ensemble, these quantities are determined from the dipole fits to the form factor data described in the previous subsection.

In order to compare these results with experiment at the physical pion mass, which is 134.8 MeV in the isospin limit [70], we perform extrapolations employing physically well-motivated functional forms taken from chiral perturbation theory (ChPT). Rather than attempting a fully *ab initio* prediction of nucleon observables, we make use of ChPT with parameters input from phenomenology; the compatibility of the lattice data with the phenomenological fit forms corroborates the validity of the extrapolations. To observe the congruence with ChPT, we include a certain limited range of data, namely, the first four ensembles listed in Tab. I, which are those with the smallest pion masses and largest lattice volumes; by confining the fits to this region, we concentrate on the regime where the predictions of ChPT are most significant. Details of the extrapolations are given in Appendix A. We note that more recent works in chiral effective theory [71–75] have also included the infinite-volume extrapolation, however we do not attempt to apply them here.

#### 1. Isovector Dirac radius $(r_1^2)^v$

For each ensemble, the Dirac radius determined from a dipole fit to  $F_1^v(Q^2)$ , determined using the ratio, summation, and GPoF methods, is shown in Fig. 8. The ratio-method data show a clear trend: the computed Dirac radius increases with the source-sink separation. This indicates the presence of excited-state contamination that is still poorly controlled when using the largest source-sink separation. The dependence on source-sink separation is particularly large on the  $m_\pi = 149$  MeV ensemble; on that ensemble, the summation method yields an even larger Dirac radius.

The chiral fit form for the isovector Dirac radius has one free parameter; the fit to the summation data is of good quality and is shown in magenta in Fig. 9. Extrapolation to the physical pion mass produces good agreement with the experimental data. Although this fit is entirely compatible with our lattice data, its slope constrained by ChPT appears larger than the slope suggested by the data alone. Therefore we also perform a fit with an additional

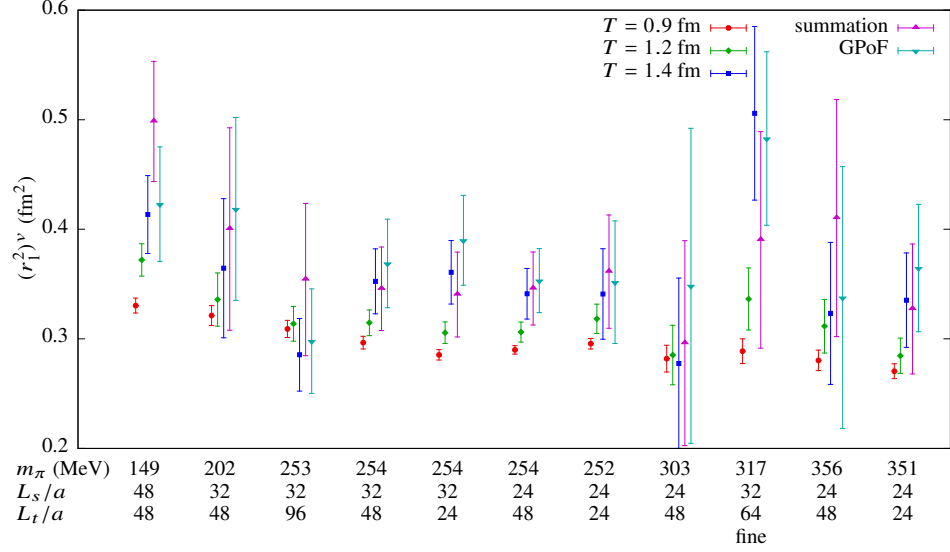


Figure 8. Isovector Dirac radius  $(r_1^2)^v$ , determined on each lattice ensemble using different analysis methods for computing form factors.

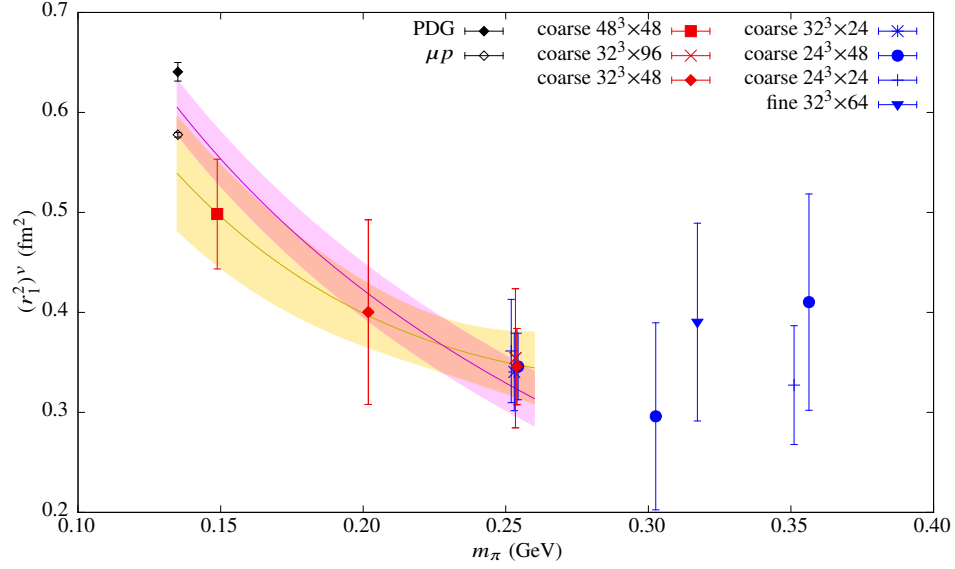


Figure 9. Chiral extrapolation of the isovector Dirac radius  $(r_1^2)^v$ , determined on each lattice ensemble using the summation method. Two experimental points are shown, where  $(r_E^2)^p$  is taken from either the CODATA 2010 result [3] used by the PDG [76] or the measurement from spectroscopy of muonic hydrogen [77]. Both points use the PDG value for  $(r_E^2)^n$ . The magenta band results from fitting with the formula from Appendix A, whereas the orange band results from including an additional term proportional to  $m_\pi^2$ .

higher-order term proportional to  $m_\pi^2$ , which is shown in orange in Fig. 9. The resulting extrapolated value has a considerably larger uncertainty, but is also consistent with both experimental points, within  $1-2\sigma$ .

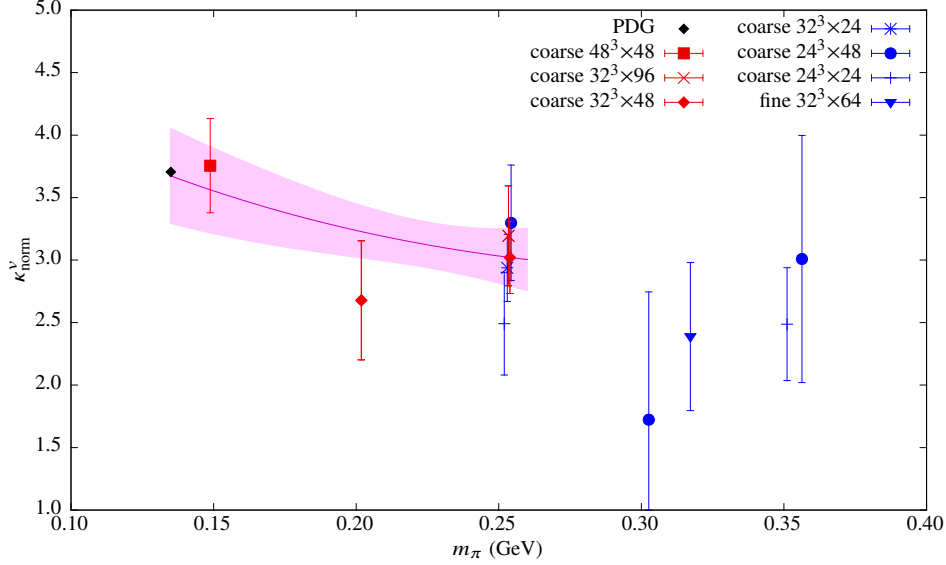


Figure 10. Chiral extrapolation of the isovector anomalous magnetic moment  $\kappa_{\text{norm}}^v$ , determined on each lattice ensemble using the summation method. The experimental point is from the PDG [76]

## 2. Isovector anomalous magnetic moment $\kappa^v$

For comparing across different ensembles, we normalize the isovector anomalous magnetic moment relative to the physical magneton, rather than using the ensemble-dependent nucleon mass as in Eq. (1):

$$\kappa_{\text{norm}}^v = \frac{m_N^{\text{phys}}}{m_N^{\text{lat}}} F_2^{v,\text{lat}}(0). \quad (25)$$

As shown in Fig. 10, the summation method on the  $m_\pi = 149$  MeV ensemble produces a value of  $\kappa^v$  consistent with experiment, as does the two-parameter chiral extrapolation to the physical pion mass. We only find a clear sign of excited-state effects on the  $m_\pi = 149$  MeV ensemble; see Appendix B.

## 3. Isovector Pauli radius $(r_2^2)^v$

For chiral extrapolation, it is more natural to use the combination  $\kappa^v(r_2^2)^v$ . As shown in Fig. 11, when using the summation method, this quantity on the  $m_\pi = 149$  MeV ensemble is consistent with the experimental points, as is the value obtained using the one-parameter extrapolation to the physical pion mass. Excited-state effects for the Pauli radius are similar to those for the anomalous magnetic moment; see Appendix B.

## IV. ISOSCALAR FORM FACTORS

We also compute isoscalar form factors. Since we do not include the contributions from disconnected quark contractions, these results suffer from an uncontrolled systematic error. Despite this, these results are still useful for illustrating qualitative features and the effects of other systematic errors. They will also give some insight into the size of disconnected contributions.

At relatively high pion masses, light quark disconnected contributions have now been calculated directly using lattice QCD. In Ref. [78], disconnected contributions to  $G_E^p$  and  $G_M^p$  were found to be consistent with zero and at most 1% when using a pion mass of about 370 MeV. Preliminary results from a high-statistics calculation at pion mass 317 MeV find nonzero values for the disconnected contributions (positive for  $G_E$  and negative for  $G_M$ ) that are also less than 1% of the connected contribution [79].

At the physical point, total disconnected contributions have been determined using form factors from experiment together with chiral extrapolations of connected-contraction lattice data, sometimes supplemented with both experimental and lattice data on octet baryons. Using chiral perturbation theory, this is divided into strange and light

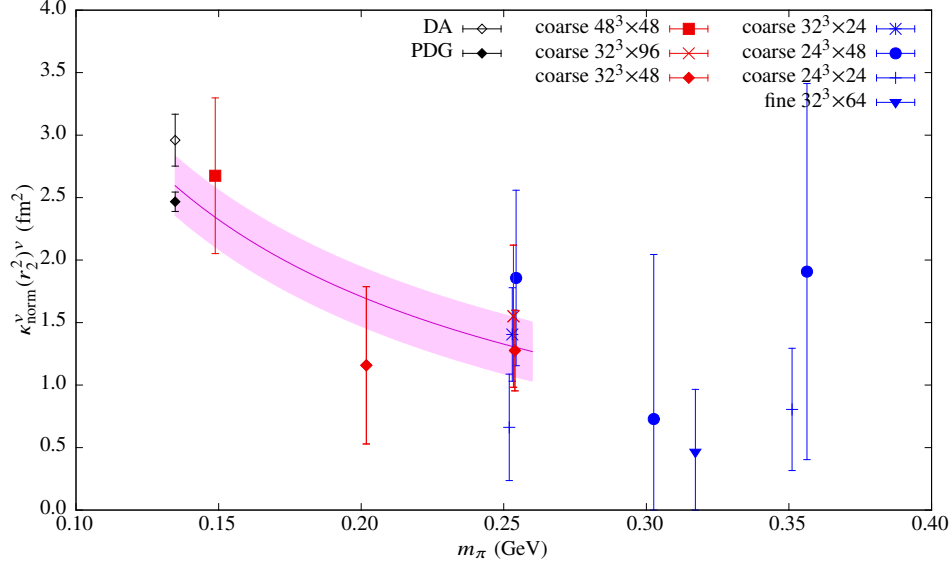


Figure 11. Chiral extrapolation of the product of the isovector anomalous magnetic moment and Pauli radius,  $\kappa_{\text{norm}}^v(r_2^2)^v$ , determined on each lattice ensemble using the summation method. We show two experimental values, where the radii are taken either from the 2012 PDG [76] or from the dispersion analysis in Ref. [10] (the difference mostly comes from different values for the proton magnetic radius).

quark contributions, in order to obtain the strange quark contribution alone, which is presented in Refs. [80–83]. Most precisely determined is the disconnected contribution to  $G_M^p(0)$ , where experimental data on octet baryon magnetic moments were used; taking the result from Ref. [83] and undoing the division into strange and light contributions yields a roughly  $-3\%$  disconnected contribution, with a 20% relative uncertainty on the estimate. At  $Q^2 = 0.26 \text{ GeV}^2$ , the disconnected contributions to  $G_M^p$  and  $G_E^p$  are estimated to be  $-3\%$  and  $-1.6\%$ , respectively, albeit with roughly 100% relative uncertainties in both cases.

### A. Form factors

Comparisons of the different methods for computing matrix elements, applied to the isoscalar Dirac and Pauli form factor, are in Appendix B. The isoscalar Dirac form factor behaves similarly to the isovector case, whereas the isoscalar Pauli form factor is generally consistent with zero, without any clear trends visible in the data.

#### 1. Isoscalar Dirac form factor $F_1^s(Q^2)$

As we did for the isovector Dirac form factor, we also perform dipole fits to  $F_1^s(Q^2)$  in the range  $0 \leq Q^2 < 0.5 \text{ GeV}^2$ . This produces fits of generally good quality, except on some ensembles when using the shortest source-sink separation, where the data have smaller statistical uncertainties. On the  $m_\pi = 149 \text{ MeV}$  ensemble, these data suffer from excited-state contamination, and the fit has  $\chi^2 = 44(13)$  for 23 degrees of freedom. As in the isovector case, it is unclear whether this level of deviation from a dipole persists when excited-state effects are reduced.

To study dependence on the fit, we vary the upper bound of the range in  $Q^2$  on three ensembles; these are shown in Fig. 12. We again find that the fit results vary by less than the statistical uncertainty and we conclude that errors caused by fitting are smaller than the statistical uncertainty.

#### 2. Isoscalar Pauli form factor $F_2^s(Q^2)$

As our isoscalar Pauli form factor data do not show a clear shape, we fit them with a line,

$$F_2^s(Q^2) = A + BQ^2, \quad (26)$$

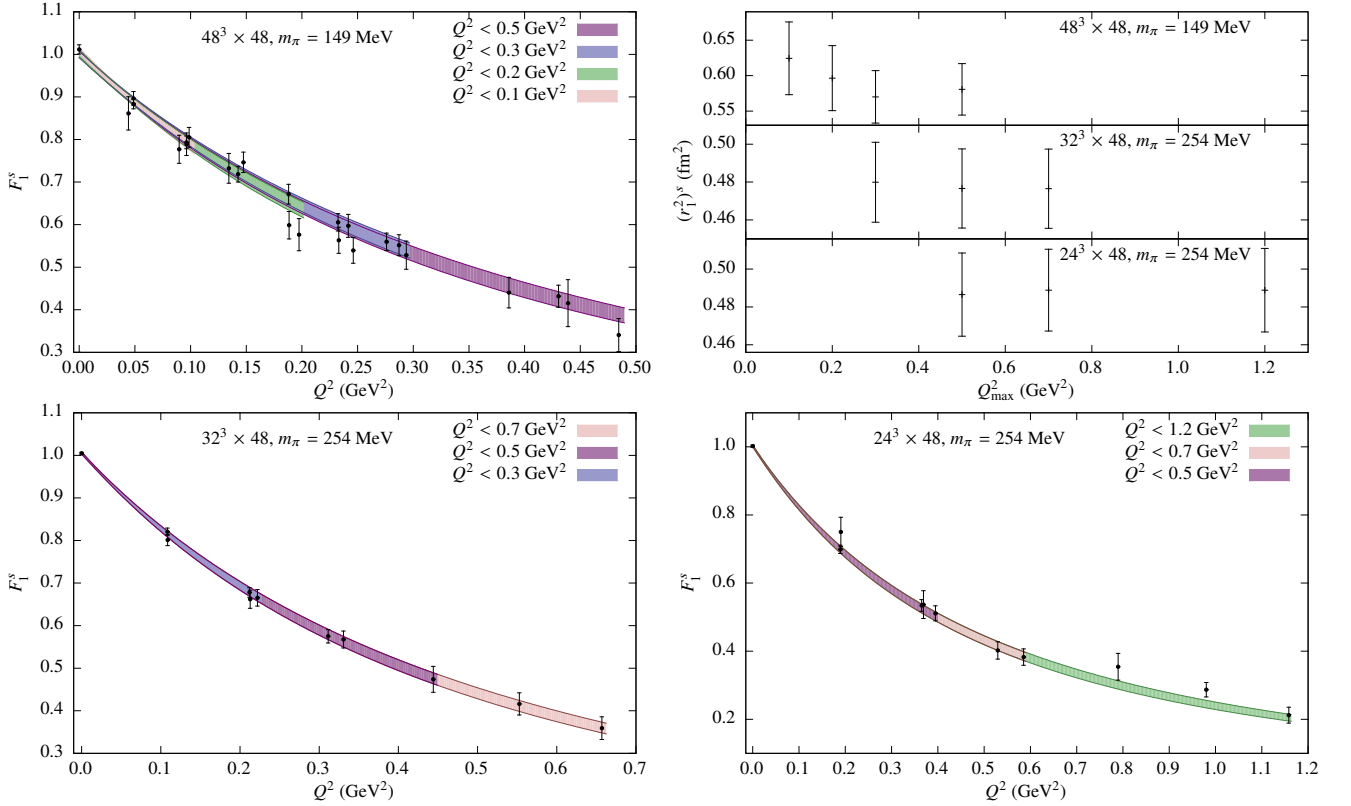


Figure 12. Dipole fits to  $F_1^s(Q^2)$  with varying  $Q_{\max}^2$ . The upper-right plot shows the dependence on  $Q_{\max}^2$  of the isoscalar Dirac radius derived from the fits.

in our standard range  $0 < Q^2 < 0.5 \text{ GeV}^2$ . The fits are generally of reasonable quality, except in some cases when using the shortest source-sink separation, such as on the  $m_\pi = 149 \text{ MeV}$  ensemble, where using the shortest source-sink separation yields  $\chi^2 = 46(13)$  for 22 degrees of freedom.

Varying, on three ensembles, the upper bound of the range of  $Q^2$  included in the fit, yields the results shown in Fig. 13. The intercept at  $Q^2 = 0$  shows a small variation with  $Q_{\max}^2$ , with a moderate increase in its statistical uncertainty as  $Q_{\max}^2$  is decreased. The slope at  $Q^2 = 0$ , which is proportional to  $\kappa^s(r_2^s)^2$ , shows a strong increase in its statistical uncertainty as  $Q_{\max}^2$  is decreased. This is caused by the  $F_2^s(Q^2)$  data being close to zero over the sampled range of  $Q^2$ , which strongly constrains a line that fits the data to have a small slope when the fitting range is wider. Although the resulting slopes are statistically consistent with the result from our choice of  $Q_{\max}^2 = 0.5 \text{ GeV}^2$ , it is clear that data that were more precise and/or at smaller  $Q^2$  could yield significantly different values for the isoscalar Pauli radius.

### 3. Isoscalar Sachs form factors

For comparison with experiment without using fits to the lattice data, we again take the Sachs electric and magnetic form factors,  $G_E$  and  $G_M$ , on the  $m_\pi = 149 \text{ MeV}$  ensemble, and compare with the parameterization of experimental data from Ref. [69]. This is shown in Fig. 14. The  $G_E$  data are in fairly good agreement with the curve, whereas the  $G_M$  data tend to lie somewhat above the curve. It should be noted that, as computed at  $m_\pi = 317 \text{ MeV}$ , disconnected  $G_M$  is negative [79], so adding it would bring the data closer to the curve, although the tendency for  $G_M$  to be high could be caused by other sources, including statistical noise. Quantitatively, we find  $p = 0.25$  for  $G_E$  and  $p = 0.47$  for  $G_M$ , which are smaller than we found for the isovector case. We should expect worse agreement with experiment due to the absence of contributions from disconnected quark contractions, but the fact that the data are still fairly close to experiment suggests that the disconnected contributions are not large.



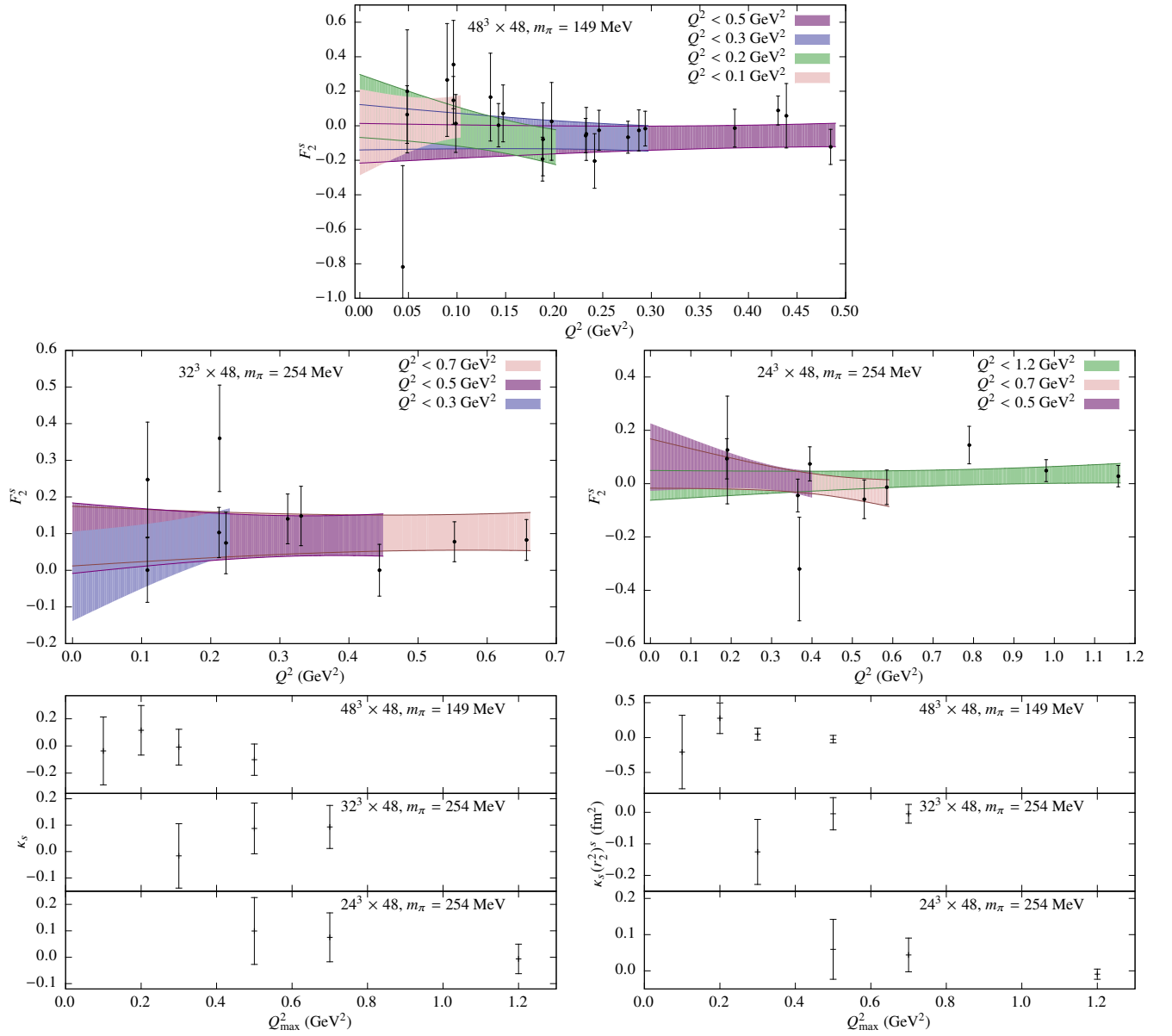


Figure 13. Line fits to  $F_2^s(Q^2)$  with varying  $Q^2_{\max}$ . The last two plots show the dependence on  $Q^2_{\max}$  of the fit parameters.

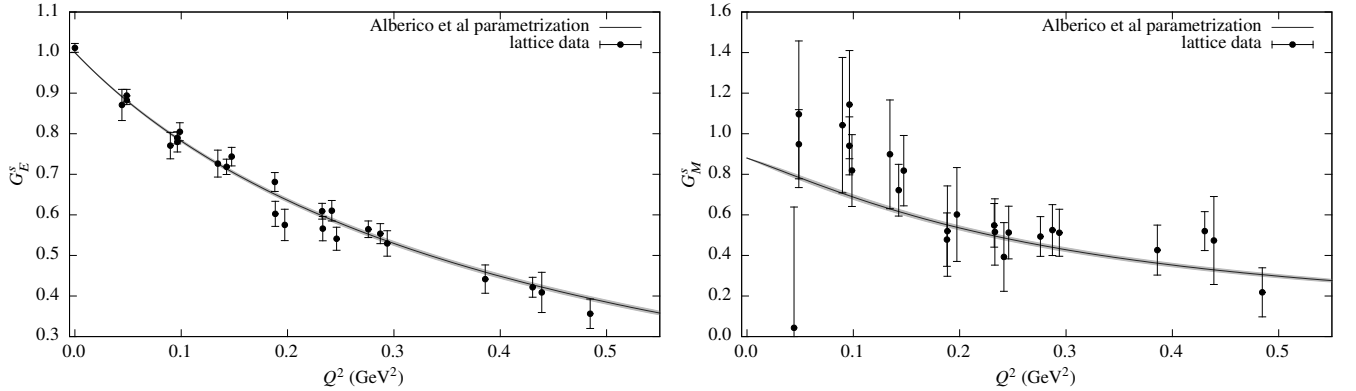


Figure 14. Isoscalar electric and magnetic form factors. Each plot contains the curve with error band from the fit to experiment in Ref. [69] and the summation data from the  $m_\pi = 149$  MeV ensemble.

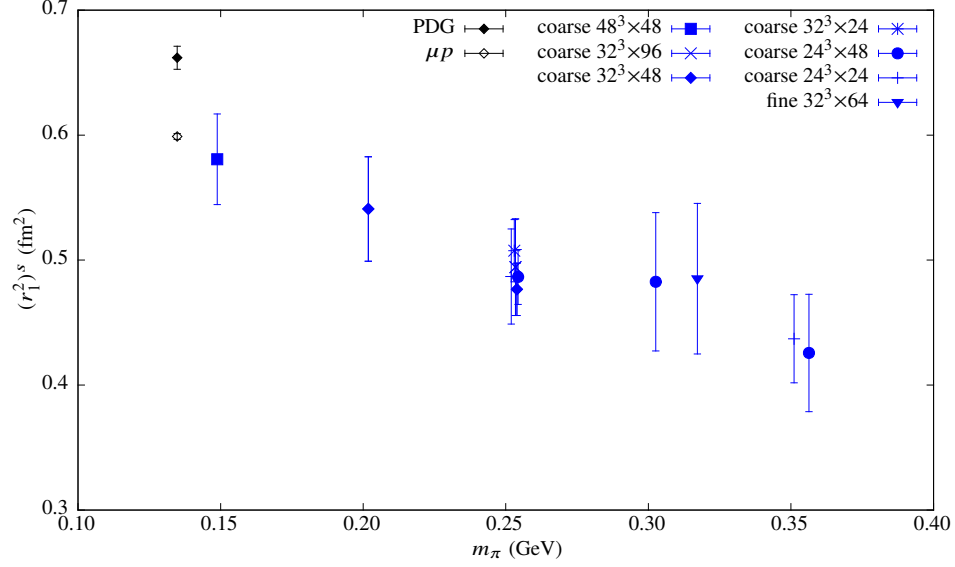


Figure 15. Isoscalar Dirac radius  $(r_1^2)^s$ , determined on each lattice ensemble using the summation method. Two experimental points are shown, where  $(r_E^2)^p$  is taken from either the CODATA 2010 result [3] used by the PDG [76] or the measurement from spectroscopy of muonic hydrogen [77]. Both points use the PDG value for  $(r_E^2)^n$ .

## B. Isoscalar Radii and magnetic moment

The isoscalar Dirac and Pauli radii  $(r_{1,2}^2)^s$ , and the isoscalar anomalous magnetic moment are related to the behavior of  $F_{1,2}^s(Q^2)$  near  $Q^2 = 0$  in the same way as for the isovector case:

$$F_1^s(Q^2) = 1 - \frac{1}{6}(r_1^2)^s Q^2 + O(Q^4) \quad (27)$$

$$F_2^s(Q^2) = \kappa^s \left( 1 - \frac{1}{6}(r_2^2)^s Q^2 + O(Q^4) \right). \quad (28)$$

We again determine these quantities from the fits described in the previous section: dipole for  $F_1^s(Q^2)$  and line for  $F_2^s(Q^2)$ .

The version of chiral perturbation theory that we used for isovector observables is less useful for the isoscalar case, since, at the presently-available one-loop order, it predicts  $(r_1^2)^s$  and  $\kappa^s$  to be independent of  $m_\pi$  and  $(r_2^2)^s$  to be zero. Furthermore, the isoscalar observables are also missing contributions from disconnected diagrams, so we will not perform a careful extrapolation to the physical pion mass; instead, we will simply plot the dependence of the observables on the pion mass and compare the  $m_\pi = 149$  MeV ensemble with the experimental results.

### 1. Isoscalar Dirac radius $(r_1^2)^s$

As in the isovector case, the isoscalar Dirac radius shows significant excited-state effects, with a clear trend of increasing with the source-sink separation; see Appendix B. The summation-method results, along with the experimental data, are plotted versus the pion mass in Fig. 15. As the pion mass decreases, the isoscalar Dirac radius increases, and the result from the  $m_\pi = 149$  MeV ensemble is consistent with the lower experimental point. The multiple ensembles at  $m_\pi \approx 250$  MeV with different volumes and temporal extents all agree well with one another, indicating the absence of significant finite-volume effects.

### 2. Isoscalar anomalous magnetic moment $\kappa^s$

As in the isovector case [Eq. (25)], we normalize the isoscalar anomalous magnetic moment to the physical magneton. The results are shown in Fig. 16 and in Appendix B. There is no clear, consistent sign of significant excited-state effects

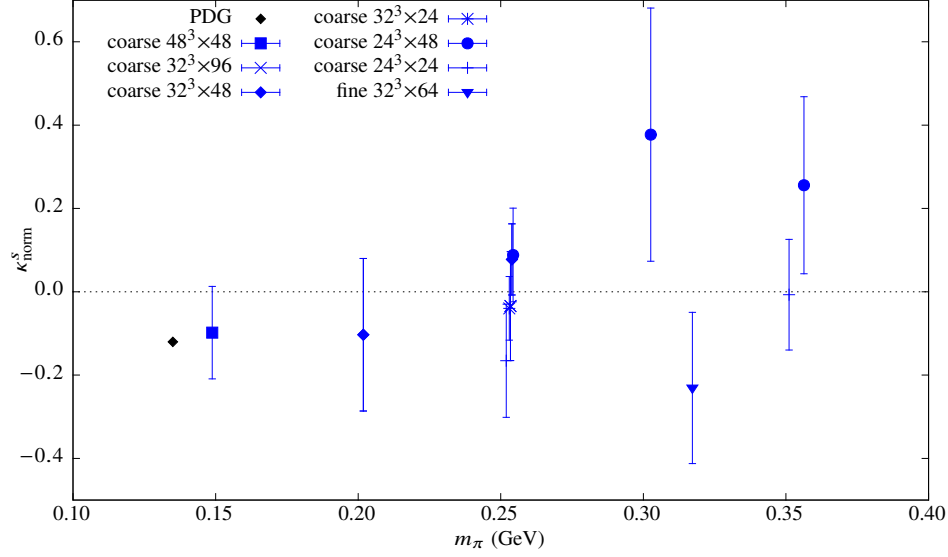


Figure 16. Isoscalar anomalous magnetic moment  $\kappa_{\text{norm}}^s$ , determined on each lattice ensemble using the summation method.

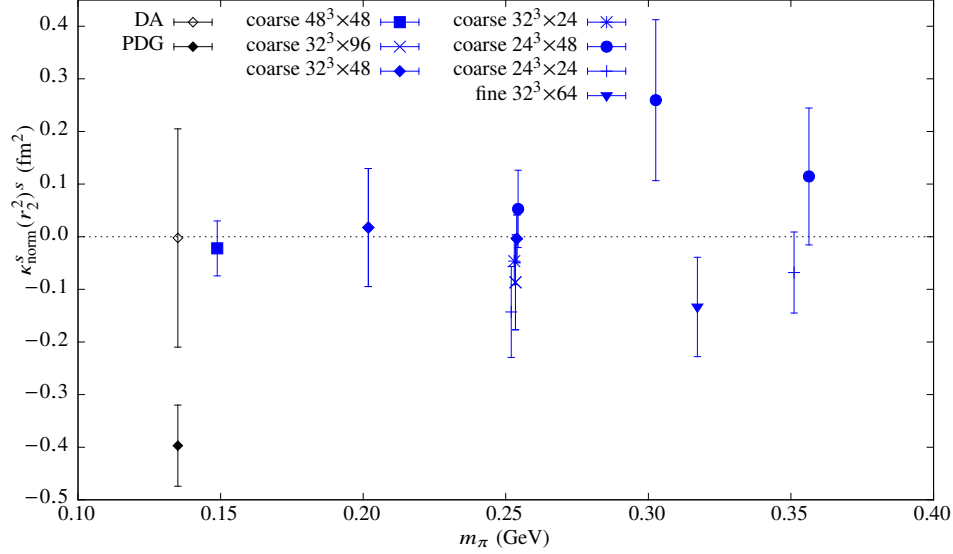


Figure 17. Product of the isoscalar anomalous magnetic moment and Pauli radius,  $\kappa_{\text{norm}}^s(r_2^2)^s$ , determined on each lattice ensemble using the summation method. We show two experimental values, where the radii are taken either from the 2012 PDG [76] or from the dispersion analysis in Ref. [10] (the difference mostly comes from different values for the proton magnetic radius).

or a dependence on the pion mass. The  $m_\pi = 149$  MeV ensemble is consistent with the experimental measurement, albeit with a 100% statistical uncertainty.

### 3. Isoscalar Pauli radius $(r_2^2)^s$

Because  $\kappa^s$  is poorly determined from our fits to  $F_2^s(Q^2)$ , the combination  $\kappa^s(r_2^2)^s$ , which is simply proportional to the slope of  $F_2^s$  at  $Q^2 = 0$ , is better to work with than the Pauli radius by itself. We find no clear signal of excited-state effects, as shown in Appendix B. In Fig. 17, we show the comparison with experiment. The previously-discussed tendency of the fits to produce small values for the slope of  $F_2^s(Q^2)$  leads to values of  $\kappa^s(r_2^2)^s$  that are close to zero, which is consistent with the result from dispersion-analysis fits to experimental data.

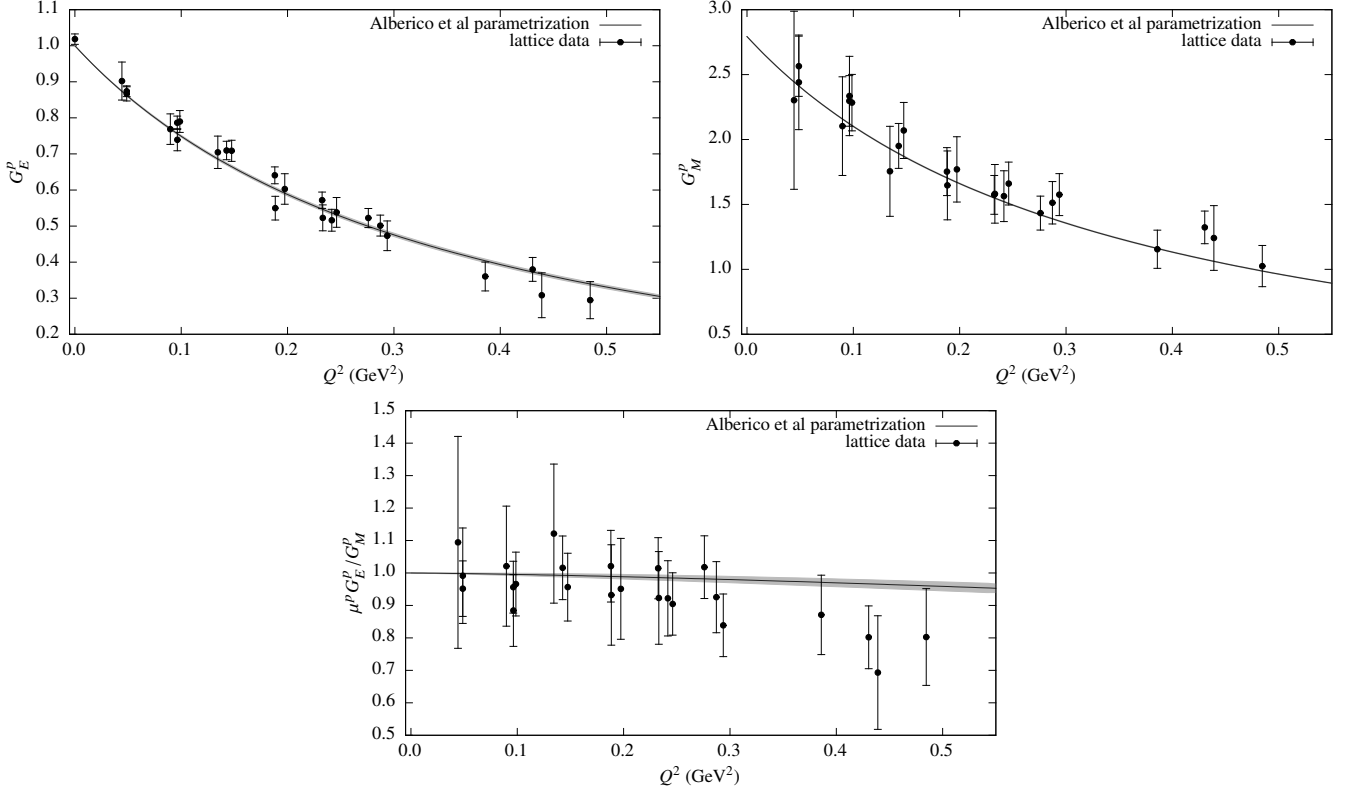


Figure 18. Proton electric and magnetic form factors, and their ratio. Each plot contains the curve with error band from the fit to experiment in Ref. [69] and the summation data from the  $m_\pi = 149$  MeV ensemble. For the third plot, the lattice values for  $\mu^p G_E^p / G_M^p$  are scaled using the proton magnetic moment from experiment, and not from the fits to lattice data.

## V. PROTON SACHS FORM FACTORS

For a final comparison with experiment, we consider the proton electric and magnetic form factors. As in the isoscalar case, the lattice data are missing the contributions from quark-disconnected diagrams, although their magnitude here is halved. Furthermore, the magnitude of the proton magnetic form factor is more than double that of the isoscalar magnetic form factor, so the relative size of disconnected contributions is even smaller.

We show the proton  $G_E$  and  $G_M$  in Fig. 18, for the summation method on the  $m_\pi = 149$  MeV ensemble. Unsurprisingly, given what we saw for the isovector and isoscalar cases in Figs. 7 and 14, there is again good agreement between the lattice data and the parameterization of experimental data. Finally, the figure also shows the ratio  $\mu G_E / G_M$ , which is often used to probe the discrepancy between scattering experiments using Rosenbluth separation and those using polarization transfer. Although the lattice data hint at a decline at the highest  $Q^2$  probed on this ensemble, as seen in the polarization transfer experiments, much higher values of  $Q^2$  are needed to settle the issue.

## VI. CONCLUSIONS

The essential result of this work is that we have achieved excellent agreement with experiment for the Sachs form factors, shown in Figs. 7, 14, and 18, and the Dirac radius, Pauli radius, and magnetic moment, as summarized in Tab. II. This was achieved by using the near-physical pion mass of 149 MeV and reducing the amount of contamination from excited states. For the Dirac radius, we found a strong signal of significant excited-state effects across all lattice ensembles, whereas for other observables these effects were most clearly seen in the  $m_\pi = 149$  MeV ensemble.

Because of the importance of controlling the systematic error due to contamination from excited states, we have studied the three methods, ratio, summation, and GPoF, and provided the most comprehensive comparison to date. We used the summation method, which is robust and widely used by the community, for our primary analysis and showed that within the present statistics, the results of all three are consistent.

The multiple ensembles with the same pion mass  $m_\pi \approx 250$  MeV and varying spatial and temporal extents  $L_s$  and

Table II. Comparison of isovector and isoscalar radii and magnetic moments with experiment. For all observables, the lattice result from the summation method on the  $m_\pi = 149$  MeV ensemble is shown, and for isovector observables the extrapolated value and the goodness-of-fit are also shown. The first set of experimental values are derived using inputs from the PDG [76], while for the second values for the Dirac radii, the proton charge radius was taken from muonic hydrogen spectroscopy [77], and for the second values for the Pauli radii, the proton and neutron radii were taken from the dispersion-analysis fits in Ref. [10].

$X$	$X_{m_\pi=149\text{ MeV}}^{\text{lat}}$	$X_{\text{extrap}}^{\text{lat}}$	$\chi^2/\text{dof}$	$X^{\text{exp}}$
$(r_1^2)^v \text{ (fm}^2\text{)}$	0.498(55)	0.605(27) <sup>a</sup>	1.7/3	0.640(9) or 0.578(2)
$\kappa^v$	3.76(38)	3.68(38)	1.8/2	3.706
$\kappa^v(r_2^2)^v \text{ (fm}^2\text{)}$	2.68(62)	2.59(24)	1.2/3	2.47(8) or 2.96(21)
$(r_1^2)^s \text{ (fm}^2\text{)}$	0.581(36)			0.662(9) or 0.599(2)
$\kappa^s$	-0.10(11)			-0.120
$\kappa^s(r_2^2)^s \text{ (fm}^2\text{)}$	-0.02(5)			-0.40(8) or 0.00(21)

<sup>a</sup> Including an additional term proportional to  $m_\pi^2$  yields an extrapolated  $(r_1^2)^v = 0.539(57) \text{ fm}^2$  with  $\chi^2/\text{dof} = 0.01/2$ .

$L_t$  allow for studying finite-volume and finite-temperature effects; we find excellent agreement for the Dirac radius between these ensembles and also good agreement for the other observables. This was reported in more detail in a separate study [84]. We also used one ensemble with a finer lattice spacing and find no sign of large discretization effects.

For the isoscalar form factors, we found similar results as in the isovector case, except that the current level of precision is insufficient for the isoscalar Pauli form factor to clearly differ from zero. Their consistency with experiment, as again summarized in Tab. II, in the absence of contributions from disconnected diagrams suggests that the latter are small. This is consistent with the size of disconnected contributions from studies with pion masses between 300 and 400 MeV and with indirect determinations at the physical point, although these also need to be calculated directly using lattice QCD close to the physical pion mass.

An important goal is an *ab initio* calculation of the proton charge radius and form factors at very low momentum transfer to help understand the origin of the apparently inconsistent experimental results. Although finite-volume and discretization effects appear to be small, confirmation at the physical pion mass is required in order to have fully-controlled systematic errors. Better control over excited-state effects is needed, ideally using several source-sink separations and very high statistics to confirm that different analysis methods converge to the same ground-state matrix elements. Finally, the determination of the derivative of  $F_1$  at  $Q^2 = 0$  needs to be better-controlled; this will be helped by the use of larger volumes which give access to  $F_1$  at smaller values of  $Q^2$ , or by the exploration of alternative techniques such as the one proposed in Ref. [85] for directly computing momentum-derivatives of matrix elements.

## ACKNOWLEDGMENTS

We thank Zoltan Fodor for useful discussions and the Budapest-Marseille-Wuppertal collaboration for making some of their configurations available to us. This research used resources of the Argonne Leadership Computing Facility at Argonne National Laboratory, which is supported by the Office of Science of the U.S. Department of Energy under contract #DE-AC02-06CH11357, and resources at Forschungszentrum Jülich.

During this research JRG, SK, JWN, AVP and SNS were supported in part by the U.S. Department of Energy Office of Nuclear Physics under grant #DE-FG02-94ER40818, ME was supported in part by DOE grant #DE-FG02-96ER40965, SNS was supported by Office of Nuclear Physics in the US Department of Energy's Office of Science under Contract #DE-AC02-05CH11231, SK was supported in part by Deutsche Forschungsgemeinschaft through grant SFB-TRR 55, and JRG was supported in part by the PRISMA Cluster of Excellence at the University of Mainz.

Calculations for this project were done using the Qlua software suite [86].

## Appendix A: Chiral extrapolation

We will largely use the same methods and phenomenological inputs for chiral perturbation theory as Refs. [44, 47]. In particular, we use the following values in the chiral limit: the pion decay constant,

$$F_\pi = 86.2 \text{ MeV}, \quad (\text{A1})$$

the delta-nucleon mass splitting,

$$\Delta = 293 \text{ MeV}, \quad (\text{A2})$$

and the nucleon axial charge,

$$g_A = 1.26. \quad (\text{A3})$$

The nucleon isovector Dirac and Pauli form factors are given in heavy baryon ChPT including the delta baryon, to order  $\epsilon^3$  in the small-scale expansion ( $\epsilon \in \{p, m_\pi, \Delta\}$ ) in Ref. [87]. This gives an expression for the Dirac radius [40],

$$\begin{aligned} (r_1^v)^2 = & -\frac{1}{(4\pi F_\pi)^2} \left[ 1 + 7g_A^2 + (2 + 10g_A^2) \log\left(\frac{m_\pi}{\lambda}\right) \right] - \frac{12B_{10}^r(\lambda)}{(4\pi F_\pi)^2} \\ & + \frac{c_A^2}{54\pi^2 F_\pi^2} \left[ 26 + 30 \log\left(\frac{m_\pi}{\lambda}\right) + 30 \frac{\Delta}{\sqrt{\Delta^2 - m_\pi^2}} \log\left(\frac{\Delta}{m_\pi} + \sqrt{\frac{\Delta^2}{m_\pi^2} - 1}\right) \right], \end{aligned} \quad (\text{A4})$$

where  $c_A$  is the leading-order pion-nucleon-delta coupling in the chiral limit, which we set to 1.5 [40], and  $B_{10}^r(\lambda)$  is a counterterm and the single free parameter.

For the anomalous magnetic moment, we include the modification from Ref. [88]:

$$\begin{aligned} \kappa^v = & \kappa_0^v - \frac{g_A^2 m_\pi m_N}{4\pi F_\pi^2} + \frac{2c_A^2 \Delta m_N}{9\pi^2 F_\pi^2} \left[ \sqrt{1 - \frac{m_\pi^2}{\Delta^2}} \log\left(\frac{\Delta}{m_\pi} + \sqrt{\frac{\Delta^2}{m_\pi^2} - 1}\right) + \log\frac{m_\pi}{2\Delta} \right] \\ & - 8E_1^r(\lambda) m_N m_\pi^2 + \frac{4c_A c_V g_A m_N m_\pi^2}{27\pi^2 F_\pi^2 \Delta} \left( 3\Delta \log\frac{2\Delta}{\lambda} + \pi m_\pi \right) \\ & - \frac{8c_A c_V g_A \Delta^2 m_N}{27\pi^2 F_\pi^2} \left[ \left(1 - \frac{m_\pi^2}{\Delta^2}\right)^{3/2} \log\left(\frac{\Delta}{m_\pi} + \sqrt{\frac{\Delta^2}{m_\pi^2} - 1}\right) + \left(1 - \frac{3m_\pi^2}{2\Delta^2}\right) \log\frac{m_\pi}{2\Delta} \right], \end{aligned} \quad (\text{A5})$$

where  $c_V$  is the leading photon-nucleon-delta coupling in the chiral limit, which we set to  $-2.5 \text{ GeV}^{-1}$ , and we use the physical nucleon mass  $m_N = 939 \text{ MeV}$ . The two free parameters are  $\kappa_0^v$  and the counterterm  $E_1^r(\lambda)$ .

The combination  $\kappa^v(r_2^v)^2$  is more natural in ChPT than the Pauli radius alone; we include the  $O(m_\pi^0)$  “core” contribution from Ref. [28] in the expression for it:

$$\kappa^v(r_2^v)^2 = \frac{g_A^2 m_N}{8\pi F_\pi^2 m_\pi} + \frac{c_A^2 m_N}{9\pi^2 F_\pi^2 \sqrt{\Delta^2 - m_\pi^2}} \log\left(\frac{\Delta}{m_\pi} + \sqrt{\frac{\Delta^2}{m_\pi^2} - 1}\right) + 24m_N \mathcal{C}, \quad (\text{A6})$$

where  $\mathcal{C}$  is the single free parameter.

## Appendix B: Additional comparisons of methods for computing matrix elements

In this appendix, we show comparisons of the ratio, summation, and GPoF methods discussed in Sec. II B to compute matrix elements, for observables where these details were omitted in the main text and for additional ensembles.

### 1. Form factors

In Fig. 19, we show the isovector Dirac and Pauli form factors for two additional ensembles, cf. Fig. 4. Signs of excited-state effects are much less clear and consistent here than they were for the two previously-shown ensembles.

Isoscalar Dirac and Pauli form factors on four ensembles are shown in Fig. 20. Increasing the source-sink separation from  $8a$  to  $10a$  tends to cause  $F_1^s$  to decrease, whereas for  $F_2^s$ , the trend is unclear. In general, the ratio method with  $T = 12a$  tends to agree with the summation and GPoF methods, except for the Dirac form factor on the  $m_\pi = 149 \text{ MeV}$  ensemble, where the summation method produces results that generally lie below the others. This suggests that, as for the isovector form factors, excited-state effects are small except at the lightest pion mass.

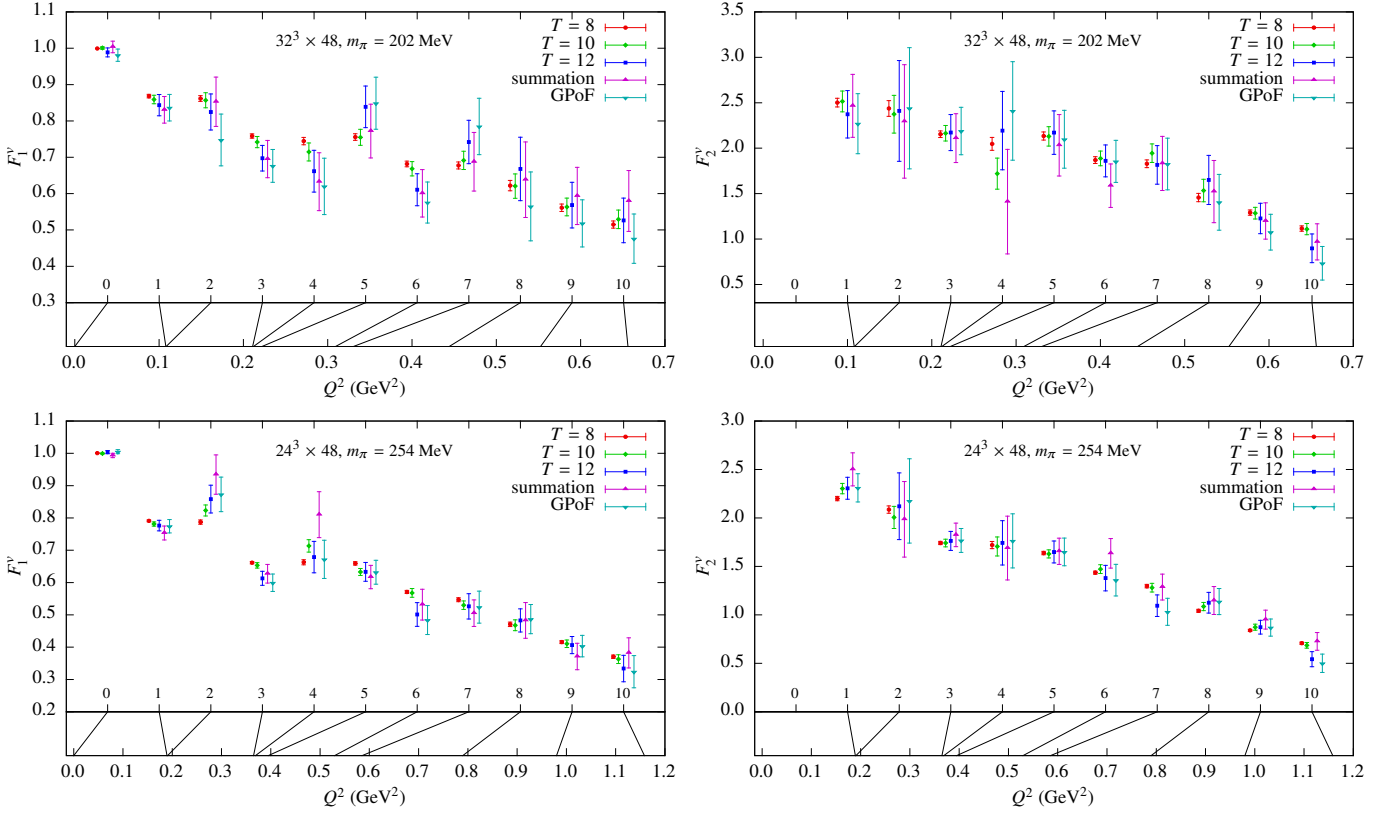


Figure 19. Comparison of different methods to extract the ground state isovector form factors  $F_1^v(Q^2)$  and  $F_2^v(Q^2)$ . The upper plots show the  $m_\pi = 202$  MeV ensemble and the lower plots show the  $m_\pi = 254$  MeV,  $24^3 \times 48$  ensemble.

## 2. Radii and magnetic moments

The isovector anomalous magnetic moment,  $\kappa_{\text{norm}}^v$ , is shown in Fig. 21. There is no broad trend of dependence on source-sink separation, except at the lightest pion mass, where the extracted magnetic moment increases with the source-sink separation, and the summation method produces a still-higher value.

For the isovector Pauli radius, we show the dependence on the method used for computing matrix elements in Fig. 22. The result is very similar to  $\kappa^v$ : there is no broad trend of dependence on source-sink separation, but  $(r_2^2)^v$  does appear to increase with source-sink separation on the  $m_\pi = 149$  MeV ensemble, and the summation method produces a still-higher value.

In Figs. 23–25, we show the isoscalar radii and anomalous magnetic moment. These behave similarly to the isovector case: we find large excited-state effects for the Dirac radius but not for observables related to the Pauli form factor at  $Q^2 = 0$ .

## Appendix C: Tables of results

We list isovector and isoscalar Dirac and Pauli form factors for four ensembles, computed using the summation method, in Tabs. III–VI.

- 
- [1] M. Burkardt, Phys. Rev. D **62**, 071503 (2000), arXiv:hep-ph/0005108.
  - [2] M. Burkardt, Int. J. Mod. Phys. A **18**, 173 (2003), arXiv:hep-ph/0207047.
  - [3] P. J. Mohr, B. N. Taylor, and D. B. Newell, Rev. Mod. Phys. **84**, 1527 (2012), arXiv:1203.5425 [physics.atom-ph].
  - [4] R. Pohl, A. Antognini, F. Nez, F. D. Amaro, F. Biraben, *et al.*, Nature **466**, 213 (2010).
  - [5] J. Friedrich and T. Walcher, Eur. Phys. J. A **17**, 607 (2003), arXiv:hep-ph/0303054.

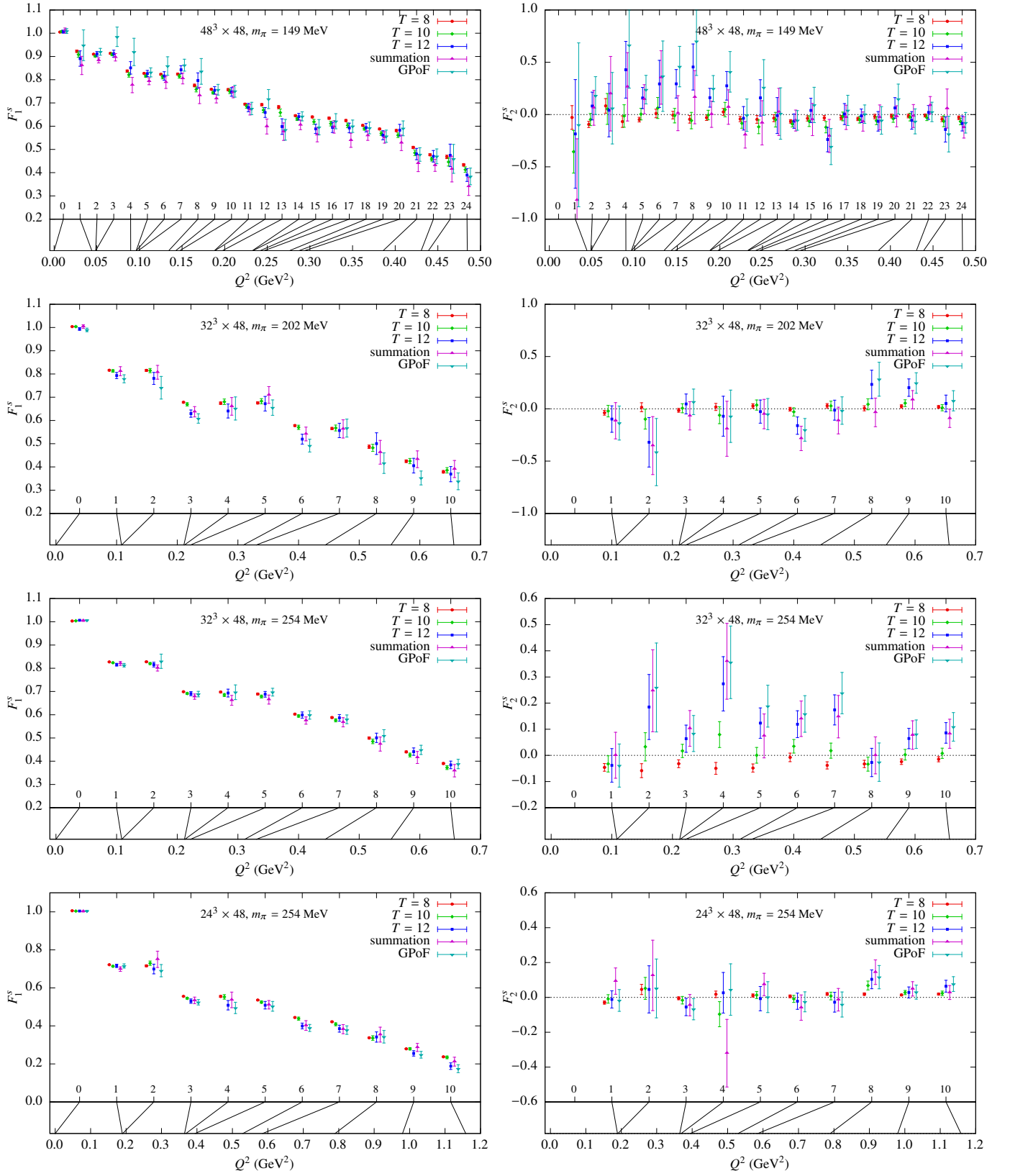


Figure 20. Comparison of different methods to extract the connected-quark-contraction contribution to the ground state isoscalar form factors  $F_1^s(Q^2)$  and  $F_2^s(Q^2)$ . From top to bottom, data from the  $m_\pi = 149$  MeV, 202 MeV, 254 MeV ( $32^3 \times 48$ ), and 254 MeV ( $24^3 \times 48$ ) lattice ensembles are shown.



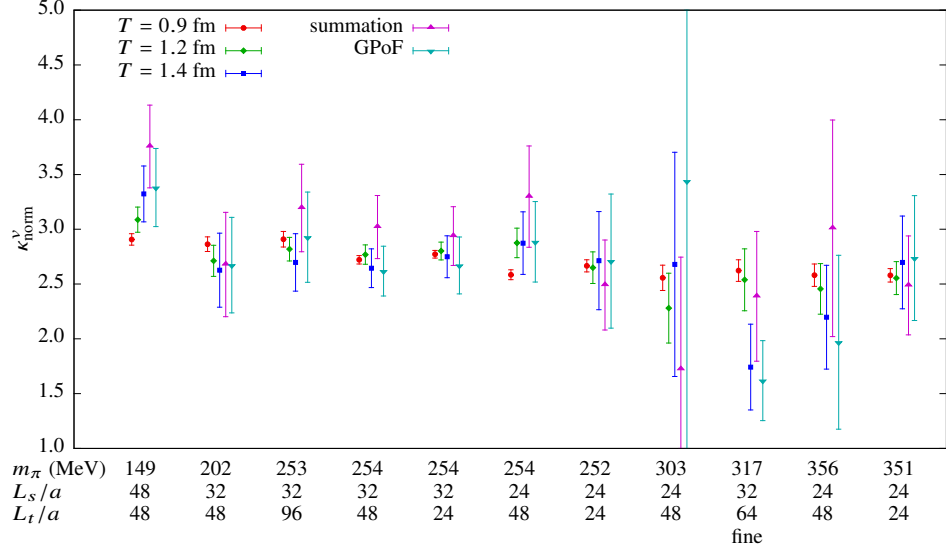


Figure 21. Isovector anomalous magnetic moment  $\kappa_{\text{norm}}^v$ , determined on each lattice ensemble using different analysis methods for computing form factors.

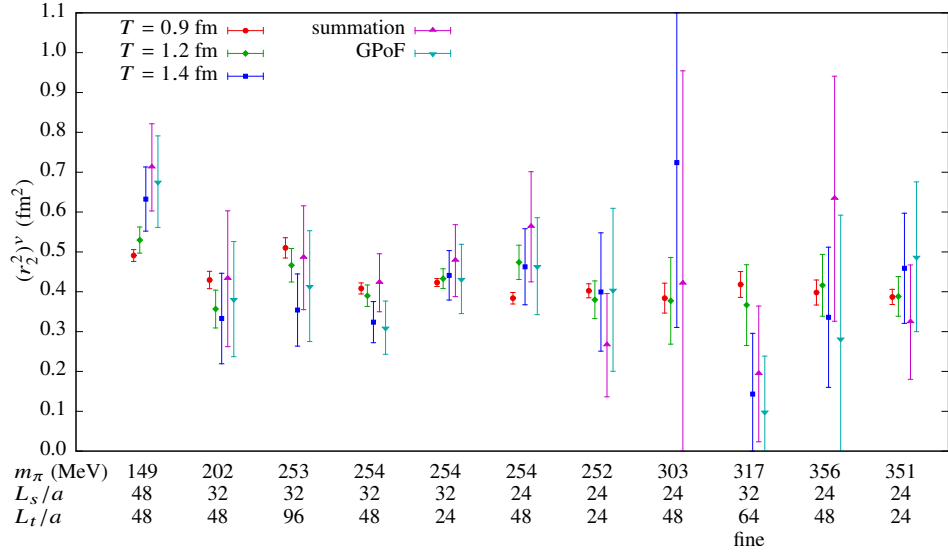


Figure 22. Isovector Pauli radius  $(r_2^2)^v$ , determined on each lattice ensemble using different analysis methods for computing form factors.

- [6] J. Arrington, W. Melnitchouk, and J. A. Tjon, Phys. Rev. C **76**, 035205 (2007), arXiv:0707.1861 [nucl-ex].
- [7] G. Hohler, E. Pietarinen, I. Sabha Stefanescu, F. Borkowski, G. G. Simon, *et al.*, Nucl. Phys. B **114**, 505 (1976).
- [8] P. Mergell, U.-G. Meißner, and D. Drechsel, Nucl. Phys. A **596**, 367 (1996), arXiv:hep-ph/9506375.
- [9] M. A. Belushkin, H.-W. Hammer, and U.-G. Meißner, Phys. Rev. C **75**, 035202 (2007), arXiv:hep-ph/0608337 [hep-ph].
- [10] I. T. Lorenz, H.-W. Hammer, and U.-G. Meißner, Eur. Phys. J. A **48**, 151 (2012), arXiv:1205.6628 [hep-ph].
- [11] B. D. Milbrath *et al.* (Bates FPP collaboration), Phys. Rev. Lett. **80**, 452 (1998), arXiv:nucl-ex/9712006.
- [12] T. Pospischil *et al.* (A1 Collaboration), Eur. Phys. J. A **12**, 125 (2001).
- [13] O. Gayou *et al.* (Jefferson Lab Hall A Collaboration), Phys. Rev. Lett. **88**, 092301 (2002), arXiv:nucl-ex/0111010.
- [14] O. Gayou, K. Wijesooriya, A. Afanasev, M. Amarian, K. Aniol, *et al.*, Phys. Rev. C **64**, 038202 (2001).
- [15] V. Punjabi, C. F. Perdrisat, K. A. Aniol, F. T. Baker, J. Berthot, *et al.*, Phys. Rev. C **71**, 055202 (2005), arXiv:nucl-ex/0501018.
- [16] R. P. Bennett, AIP Conf. Proc. **1441**, 156 (2012).
- [17] M. Moteabbed *et al.* (CLAS Collaboration), Phys. Rev. C **88**, 025210 (2013), arXiv:1306.2286 [nucl-ex].

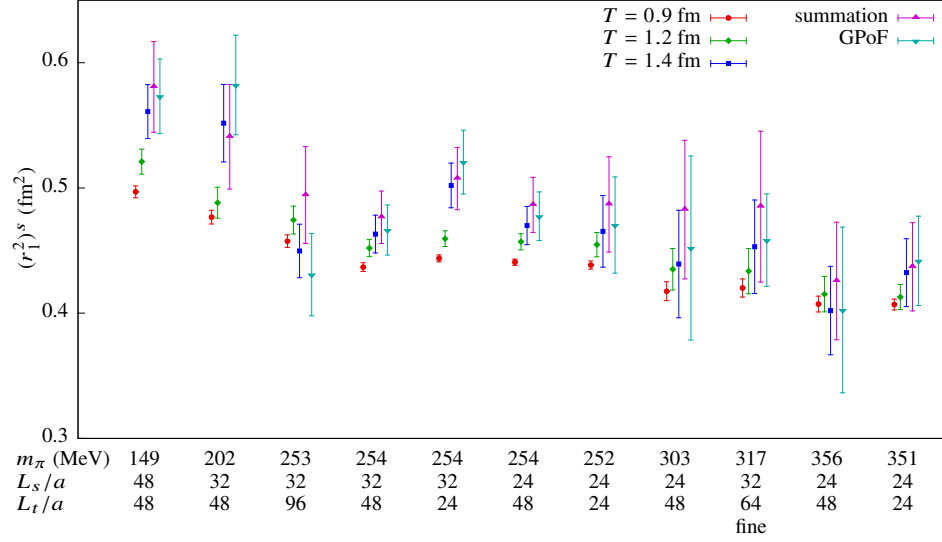


Figure 23. Isoscalar Dirac radius  $(r_1^2)^s$ , determined on each lattice ensemble using different analysis methods for computing form factors.

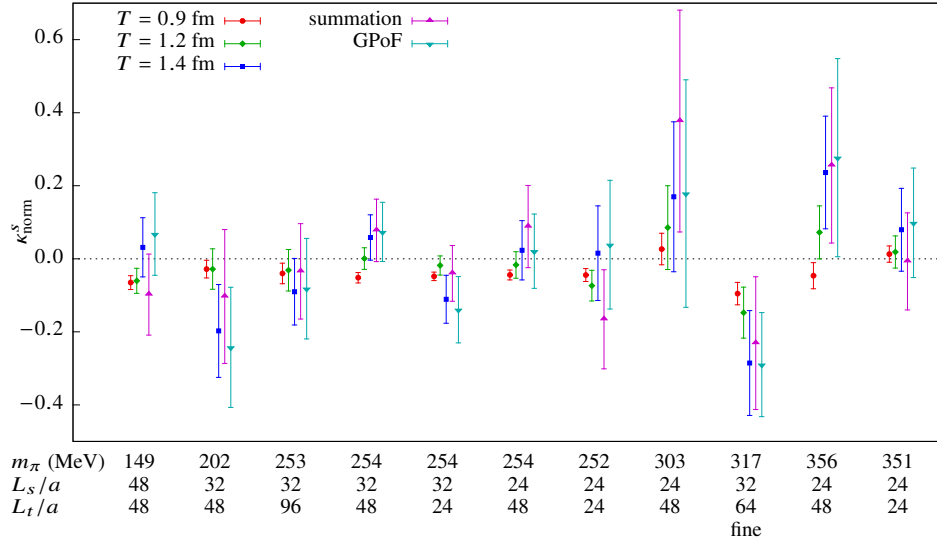


Figure 24. Isoscalar anomalous magnetic moment  $\kappa_{\text{norm}}^s$ , determined on each lattice ensemble using different analysis methods for computing form factors.

- [18] A. V. Gramolin, J. Arrington, L. M. Barkov, V. F. Dmitriev, V. V. Gauzshtein, *et al.*, Nucl. Phys. Proc. Suppl. **225-227**, 216 (2012), arXiv:1112.5369 [nucl-ex].
- [19] D. M. Nikolenko *et al.*, EPJ Web of Conferences **66**, 06002 (2014).
- [20] R. G. Milner (OLYMPUS Collaboration), AIP Conf. Proc. **1441**, 159 (2012).
- [21] R. Milner *et al.* (OLYMPUS Collaboration), Nuclear Inst. and Methods in Physics Research, A **741**, 1 (2014), arXiv:1312.1730 [physics.ins-det].
- [22] J. Arrington, C. D. Roberts, and J. M. Zanotti, J. Phys. G **34**, S23 (2007), arXiv:nucl-th/0611050.
- [23] P. Hägler, Phys. Rept. **490**, 49 (2010), arXiv:0912.5483 [hep-lat].
- [24] G. Martinelli and C. T. Sachrajda, Nucl. Phys. B **316**, 355 (1989).
- [25] T. Draper, R. M. Woloshyn, and K.-F. Liu, Phys. Lett. B **234**, 121 (1990).
- [26] D. B. Leinweber, R. M. Woloshyn, and T. Draper, Phys. Rev. D **43**, 1659 (1991).
- [27] W. Wilcox, T. Draper, and K.-F. Liu, Phys. Rev. D **46**, 1109 (1992), arXiv:hep-lat/9205015.

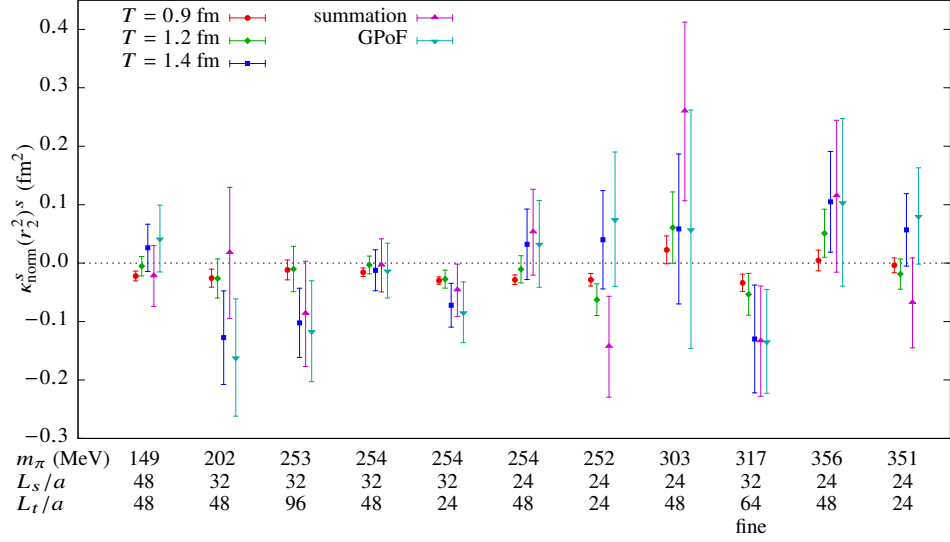


Figure 25. Product of the isoscalar anomalous magnetic moment and Pauli radius,  $\kappa_{\text{norm}}^s(r_2^2)^s$ , determined on each lattice ensemble using different analysis methods for computing form factors.

Table III. Electromagnetic form factors from the  $m_\pi = 149$  MeV ensemble, computed using the summation method. The first column lists representative source and sink momenta ( $\vec{p} = \frac{2\pi}{L_s}\vec{n}$  and  $\vec{p}' = \frac{2\pi}{L_s}\vec{n}'$ , respectively) for each momentum transfer  $Q^2$ .

$\langle \vec{n}'     \vec{n} \rangle$	$Q^2(\text{GeV}^2)$	Isovector		Isoscalar	
		$F_1(Q^2)$	$F_2(Q^2)$	$F_1(Q^2)$	$F_2(Q^2)$
$\langle 0, 0, 0     0, 0, 0 \rangle$	0	1.023(21)		1.012(11)	
$\langle -1, 0, 0     -2, 0, 0 \rangle$	0.044	0.974(87)	3.63(98)	0.861(39)	-0.82(59)
$\langle 0, 0, 0     1, 0, 0 \rangle$	0.049	0.913(24)	3.45(34)	0.883(11)	0.06(17)
$\langle -1, 0, 0     -1, 1, 0 \rangle$	0.049	0.883(31)	2.83(52)	0.897(16)	0.20(36)
$\langle -1, 0, 0     -2, 1, 0 \rangle$	0.090	0.866(72)	2.11(57)	0.777(33)	0.27(33)
$\langle 0, 0, 0     1, 1, 0 \rangle$	0.096	0.856(30)	2.83(28)	0.793(15)	0.15(14)
$\langle -1, 0, 0     -1, 1, 1 \rangle$	0.096	0.778(45)	2.92(40)	0.789(26)	0.35(26)
$\langle -1, 0, 0     0, 1, 0 \rangle$	0.099	0.846(44)	2.73(34)	0.805(23)	0.01(17)
$\langle -1, 0, 0     -2, 1, 1 \rangle$	0.134	0.747(73)	1.87(53)	0.732(35)	0.17(25)
$\langle 0, 0, 0     1, 1, 1 \rangle$	0.143	0.791(38)	2.39(27)	0.719(18)	0.00(13)
$\langle -1, 0, 0     0, 1, 1 \rangle$	0.147	0.782(47)	2.45(35)	0.746(24)	0.07(16)
$\langle 0, 0, 0     2, 0, 0 \rangle$	0.188	0.695(38)	2.18(27)	0.671(23)	-0.19(13)
$\langle -1, 0, 0     -1, 2, 0 \rangle$	0.188	0.598(51)	2.07(37)	0.599(32)	-0.08(21)
$\langle -1, 0, 0     1, 0, 0 \rangle$	0.197	0.745(66)	2.19(34)	0.576(38)	0.03(23)
$\langle 0, 0, 0     2, 1, 0 \rangle$	0.232	0.656(38)	1.96(21)	0.605(20)	-0.06(10)
$\langle -1, 0, 0     -1, 2, 1 \rangle$	0.233	0.600(48)	2.01(32)	0.563(31)	-0.05(15)
$\langle -1, 0, 0     0, 2, 0 \rangle$	0.242	0.605(47)	2.12(26)	0.597(27)	-0.20(16)
$\langle -1, 0, 0     1, 1, 0 \rangle$	0.246	0.661(64)	2.12(21)	0.539(30)	-0.03(12)
$\langle 0, 0, 0     2, 1, 1 \rangle$	0.276	0.614(40)	1.78(19)	0.560(20)	-0.07(9)
$\langle -1, 0, 0     0, 2, 1 \rangle$	0.287	0.598(44)	2.00(23)	0.552(25)	-0.03(12)
$\langle -1, 0, 0     1, 1, 1 \rangle$	0.294	0.564(59)	1.96(21)	0.528(33)	-0.02(10)
$\langle -1, 0, 0     1, 2, 0 \rangle$	0.386	0.466(58)	1.47(18)	0.440(36)	-0.01(11)
$\langle -1, 0, 0     1, 2, 1 \rangle$	0.430	0.481(53)	1.64(17)	0.432(26)	0.09(8)
$\langle -1, 0, 0     2, 0, 0 \rangle$	0.439	0.439(96)	1.62(33)	0.416(55)	0.06(19)
$\langle -1, 0, 0     2, 1, 0 \rangle$	0.485	0.431(87)	1.37(21)	0.341(39)	-0.12(10)

- [28] M. Göckeler, T. R. Hemmert, R. Horsley, D. Pleiter, P. E. L. Rakow, A. Schäfer, and G. Schierholz (QCDSF Collaboration), Phys. Rev. D **71**, 034508 (2005), arXiv:hep-lat/0303019.
- [29] S. J. Dong, K. F. Liu, and A. G. Williams, Phys. Rev. D **58**, 074504 (1998), arXiv:hep-ph/9712483.
- [30] A. Tang, W. Wilcox, and R. Lewis, Phys. Rev. D **68**, 094503 (2003), arXiv:hep-lat/0307006 [hep-lat].
- [31] S. Boinapalli, D. B. Leinweber, A. G. Williams, J. M. Zanotti, and J. B. Zhang, Phys. Rev. D **74**, 093005 (2006), arXiv:hep-lat/0604022 [hep-lat].

Table IV. Electromagnetic form factors from the  $m_\pi = 202$  MeV ensemble, computed using the summation method. The first column lists representative source and sink momenta ( $\vec{p} = \frac{2\pi}{L_s} \vec{n}$  and  $\vec{p}' = \frac{2\pi}{L_s} \vec{n}'$ , respectively) for each momentum transfer  $Q^2$ .

$\langle \vec{n}'     \vec{n} \rangle$	$Q^2 (\text{GeV}^2)$	Isovector		Isoscalar	
		$F_1(Q^2)$	$F_2(Q^2)$	$F_1(Q^2)$	$F_2(Q^2)$
$\langle 0, 0, 0     0, 0, 0 \rangle$	0	1.004(16)		1.004(8)	
$\langle 0, 0, 0     1, 0, 0 \rangle$	0.108	0.831(37)	2.47(35)	0.812(19)	-0.11(17)
$\langle -1, 0, 0     -1, 1, 0 \rangle$	0.108	0.853(68)	2.29(62)	0.807(30)	-0.35(28)
$\langle 0, 0, 0     1, 1, 0 \rangle$	0.211	0.695(51)	2.11(27)	0.637(22)	-0.07(14)
$\langle -1, 0, 0     -1, 1, 1 \rangle$	0.212	0.633(80)	1.41(57)	0.661(38)	-0.19(26)
$\langle -1, 0, 0     0, 1, 0 \rangle$	0.222	0.772(74)	2.03(34)	0.710(36)	-0.05(14)
$\langle 0, 0, 0     1, 1, 1 \rangle$	0.309	0.601(65)	1.59(24)	0.542(29)	-0.28(12)
$\langle -1, 0, 0     0, 1, 1 \rangle$	0.330	0.688(81)	1.83(30)	0.564(39)	-0.11(13)
$\langle -1, 0, 0     1, 0, 0 \rangle$	0.444	0.638(104)	1.52(34)	0.463(51)	-0.03(14)
$\langle -1, 0, 0     1, 1, 0 \rangle$	0.552	0.594(79)	1.20(20)	0.433(36)	0.09(9)
$\langle -1, 0, 0     1, 1, 1 \rangle$	0.656	0.580(84)	0.97(20)	0.391(37)	-0.09(9)

Table V. Electromagnetic form factors from the  $m_\pi = 254$  MeV,  $32^3 \times 48$  ensemble, computed using the summation method. Source and sink momenta are the same as given in Tab. IV.

$Q^2 (\text{GeV}^2)$	Isovector		Isoscalar	
	$F_1(Q^2)$	$F_2(Q^2)$	$F_1(Q^2)$	$F_2(Q^2)$
0	1.007(6)		1.005(3)	
0.108	0.849(18)	2.72(23)	0.821(9)	0.00(9)
0.109	0.893(30)	3.01(36)	0.801(13)	0.25(16)
0.212	0.751(24)	2.51(17)	0.678(11)	0.10(7)
0.213	0.800(44)	2.84(32)	0.662(21)	0.36(15)
0.222	0.711(38)	2.16(20)	0.665(19)	0.07(8)
0.311	0.686(33)	2.34(16)	0.575(16)	0.14(7)
0.331	0.666(39)	1.95(17)	0.567(20)	0.15(8)
0.444	0.478(57)	1.51(17)	0.474(30)	0.00(7)
0.553	0.464(43)	1.27(13)	0.416(26)	0.08(5)
0.657	0.409(44)	1.08(13)	0.359(27)	0.08(6)

- [32] C. Alexandrou, G. Koutsou, J. W. Negele, and A. Tsapalis, Phys. Rev. D **74**, 034508 (2006), arXiv:hep-lat/0605017.  
[33] M. Göckeler *et al.* (QCDSF/UKQCD Collaboration), PoS **LAT2007**, 161 (2007), arXiv:0710.2159 [hep-lat].  
[34] S. Collins, M. Göckeler, P. Hägler, R. Horsley, Y. Nakamura, *et al.*, Phys. Rev. D **84**, 074507 (2011), arXiv:1106.3580 [hep-lat].  
[35] H.-W. Lin, T. Blum, S. Ohta, S. Sasaki, and T. Yamazaki, Phys. Rev. D **78**, 014505 (2008), arXiv:0802.0863 [hep-lat].  
[36] C. Alexandrou, Chin. Phys. C **33**, 1093 (2009), arXiv:0906.4137 [hep-lat].  
[37] C. Alexandrou, M. Brinet, J. Carbonell, M. Constantinou, P. A. Harraud, *et al.*, Phys. Rev. D **83**, 094502 (2011), arXiv:1102.2208 [hep-lat].

Table VI. Electromagnetic form factors from the  $m_\pi = 254$  MeV,  $24^3 \times 48$  ensemble, computed using the summation method. Source and sink momenta are the same as given in Tab. IV, scaled by 4/3 due to the smaller box size.

$Q^2 (\text{GeV}^2)$	Isovector		Isoscalar	
	$F_1(Q^2)$	$F_2(Q^2)$	$F_1(Q^2)$	$F_2(Q^2)$
0	0.993(7)		1.002(3)	
0.189	0.753(21)	2.50(17)	0.699(12)	0.09(8)
0.190	0.934(61)	1.99(39)	0.750(43)	0.13(20)
0.365	0.627(29)	1.83(12)	0.534(17)	-0.04(6)
0.369	0.810(71)	1.69(33)	0.537(41)	-0.32(19)
0.395	0.617(36)	1.66(14)	0.511(22)	0.07(6)
0.529	0.532(48)	1.63(15)	0.402(25)	-0.06(7)
0.585	0.505(41)	1.29(13)	0.383(24)	-0.01(6)
0.790	0.483(55)	1.15(14)	0.354(39)	0.14(7)
0.980	0.371(41)	0.95(10)	0.287(21)	0.05(4)
1.158	0.382(47)	0.73(9)	0.212(23)	0.03(4)

- [38] P. E. Shanahan, A. W. Thomas, R. D. Young, J. M. Zanotti, R. Horsley, *et al.*, Phys. Rev. D **89**, 074511 (2014), arXiv:1401.5862 [hep-lat].
- [39] P. E. Shanahan, A. W. Thomas, R. D. Young, J. M. Zanotti, R. Horsley, *et al.*, Phys. Rev. D **90**, 034502 (2014), arXiv:1403.1965 [hep-lat].
- [40] S. N. Syritsyn, J. D. Bratt, M. F. Lin, H. B. Meyer, J. W. Negele, *et al.*, Phys. Rev. D **81**, 034507 (2010), arXiv:0907.4194 [hep-lat].
- [41] T. Yamazaki, Y. Aoki, T. Blum, H.-W. Lin, S. Ohta, *et al.*, Phys. Rev. D **79**, 114505 (2009), arXiv:0904.2039 [hep-lat].
- [42] M. Lin, PoS **LATTICE2013**, 275 (2013), arXiv:1401.1476 [hep-lat].
- [43] P. Hägler *et al.* (LHPC Collaboration), Phys. Rev. D **77**, 094502 (2008), arXiv:0705.4295 [hep-lat].
- [44] J. D. Bratt, R. G. Edwards, M. Engelhardt, P. Hägler, H. W. Lin, *et al.* (LHPC Collaboration), Phys. Rev. D **82**, 094502 (2010), arXiv:1001.3620 [hep-lat].
- [45] C. Alexandrou, M. Constantinou, S. Dinter, V. Drach, K. Jansen, *et al.*, Phys. Rev. D **88**, 014509 (2013), arXiv:1303.5979 [hep-lat].
- [46] T. Bhattacharya, S. D. Cohen, R. Gupta, A. Joseph, H.-W. Lin, *et al.*, Phys. Rev. D **89**, 094502 (2014), arXiv:1306.5435 [hep-lat].
- [47] J. R. Green, M. Engelhardt, S. Krieg, J. W. Negele, A. V. Pochinsky, *et al.*, Phys. Lett. B **734**, 290 (2014), arXiv:1209.1687 [hep-lat].
- [48] S. Capitani, M. Della Morte, G. von Hippel, B. Jäger, B. Knippschild, *et al.*, PoS **LATTICE2012**, 177 (2012), arXiv:1211.1282 [hep-lat].
- [49] B. Jäger, T. D. Rae, S. Capitani, M. Della Morte, D. Djukanovic, *et al.*, PoS **Lattice 2013**, 272 (2013), arXiv:1311.5804 [hep-lat].
- [50] S. Capitani, S. Dürr, and C. Hoelbling, JHEP **0611**, 028 (2006), arXiv:hep-lat/0607006.
- [51] S. Dürr, Z. Fodor, C. Hoelbling, S. Katz, S. Krieg, *et al.*, JHEP **1108**, 148 (2011), arXiv:1011.2711 [hep-lat].
- [52] S. R. Beane, W. Detmold, T. C. Luu, K. Orginos, A. Parreno, *et al.*, Phys. Rev. D **79**, 114502 (2009), arXiv:0903.2990 [hep-lat].
- [53] S. Güsken, Nucl. Phys. Proc. Suppl. **17**, 361 (1990).
- [54] G. P. Lepage, in *From Actions to Answers: Proceedings of the 1989 Theoretical Advanced Study Institute in Elementary Particle Physics, 5–30 June 1989, University of Colorado, Boulder*, edited by T. DeGrand and D. Toussaint (1989) pp. 97–120.
- [55] S. Capitani, B. Knippschild, M. Della Morte, and H. Wittig, PoS **LATTICE2010**, 147 (2010), arXiv:1011.1358 [hep-lat].
- [56] J. Bulava, M. A. Donnellan, and R. Sommer (ALPHA Collaboration), PoS **LATTICE2010**, 303 (2010), arXiv:1011.4393 [hep-lat].
- [57] M. Lüscher and U. Wolff, Nucl. Phys. B **339**, 222 (1990).
- [58] B. Blossier, M. Della Morte, G. von Hippel, T. Mendes, and R. Sommer, JHEP **0904**, 094 (2009), arXiv:0902.1265 [hep-lat].
- [59] C. Aubin and K. Orginos, AIP Conf. Proc. **1374**, 621 (2011), arXiv:1010.0202 [hep-lat].
- [60] S. Capitani, M. Della Morte, G. von Hippel, B. Jäger, A. Jüttner, *et al.*, Phys. Rev. D **86**, 074502 (2012), arXiv:1205.0180 [hep-lat].
- [61] J. Green, J. Negele, A. Pochinsky, S. Krieg, and S. Syritsyn, PoS **LATTICE2011**, 157 (2011), arXiv:1111.0255 [hep-lat].
- [62] G. S. Bali, S. Collins, B. Gläsel, M. Göckeler, J. Najjar, *et al.*, PoS **LATTICE2013**, 290 (2013), arXiv:1311.7041 [hep-lat].
- [63] G. M. von Hippel, J. Hua, B. Jäger, H. B. Meyer, T. D. Rae, and H. Wittig, PoS **LATTICE2013**, 446 (2013).
- [64] R. G. Edwards, N. Mathur, D. G. Richards, and S. J. Wallace (Hadron Spectrum Collaboration), Phys. Rev. D **87**, 054506 (2013), arXiv:1212.5236 [hep-ph].
- [65] B. J. Owen, J. Dragos, W. Kamleh, D. B. Leinweber, M. S. Mahbub, *et al.*, Phys. Lett. B **723**, 217 (2013), arXiv:1212.4668 [hep-lat].
- [66] B. J. Owen, W. Kamleh, D. B. Leinweber, M. S. Mahbub, and B. J. Menadue, PoS **LATTICE2013**, 277 (2013), arXiv:1312.0291 [hep-lat].
- [67] M. Lüscher, S. Sint, R. Sommer, P. Weisz, H. Wittig, *et al.*, Nucl. Phys. Proc. Suppl. **53**, 905 (1997), arXiv:hep-lat/9608049.
- [68] P. Hägler *et al.* (LHPC and SESAM collaborations), Phys. Rev. D **68**, 034505 (2003), arXiv:hep-lat/0304018.
- [69] W. M. Alberico, S. M. Bilenky, C. Giunti, and K. M. Graczyk, Phys. Rev. C **79**, 065204 (2009), arXiv:0812.3539 [hep-ph].
- [70] G. Colangelo, S. Dürr, A. Jüttner, L. Lellouch, H. Leutwyler, *et al.*, Eur. Phys. J. C **71**, 1695 (2011), arXiv:1011.4408 [hep-lat].
- [71] B. C. Tiburzi, Phys. Rev. D **77**, 014510 (2008), arXiv:0710.3577 [hep-lat].
- [72] L. Greil, T. R. Hemmert, and A. Schäfer, Eur. Phys. J. A **48**, 53 (2012), arXiv:1112.2539 [hep-ph].
- [73] J. M. M. Hall, D. B. Leinweber, and R. D. Young, Phys. Rev. D **85**, 094502 (2012), arXiv:1201.6114 [hep-lat].
- [74] J. M. M. Hall, D. B. Leinweber, B. J. Owen, and R. D. Young, Phys. Lett. B **725**, 101 (2013), arXiv:1210.6124 [hep-lat].
- [75] J. M. M. Hall, D. B. Leinweber, and R. D. Young, Phys. Rev. D **88**, 014504 (2013), arXiv:1305.3984 [hep-lat].
- [76] J. Beringer *et al.* (Particle Data Group), Phys. Rev. D **86**, 010001 (2012).
- [77] A. Antognini, F. Nez, K. Schuhmann, F. D. Amaro, F. Biraben, *et al.*, Science **339**, 417 (2013).
- [78] A. Abdel-Rehim, C. Alexandrou, M. Constantinou, V. Drach, K. Hadjiyiannakou, *et al.*, Phys. Rev. D **89**, 034501 (2014), arXiv:1310.6339 [hep-lat].
- [79] S. Meinel, private communication (2014).
- [80] D. B. Leinweber, S. Boinepalli, I. Cloet, A. W. Thomas, A. G. Williams, *et al.*, Phys. Rev. Lett. **94**, 212001 (2005), arXiv:hep-lat/0406002.

- [81] D. B. Leinweber, S. Boinapalli, A. W. Thomas, P. Wang, A. G. Williams, *et al.*, Phys. Rev. Lett. **97**, 022001 (2006), arXiv:hep-lat/0601025.
- [82] P. Wang, D. B. Leinweber, A. W. Thomas, and R. D. Young, Phys. Rev. C **79**, 065202 (2009), arXiv:0807.0944 [hep-ph].
- [83] P. E. Shanahan, R. Horsley, Y. Nakamura, D. Pleiter, P. E. L. Rakow, *et al.*, (2014), arXiv:1403.6537 [hep-lat].
- [84] J. Green, M. Engelhardt, S. Krieg, S. Meinel, J. Negele, *et al.*, PoS **Lattice 2013**, 276 (2013), arXiv:1310.7043 [hep-lat].
- [85] G. de Divitiis, R. Petronzio, and N. Tantalo, Phys. Lett. B **718**, 589 (2012), arXiv:1208.5914 [hep-lat].
- [86] A. Pochinsky, “Qlua,” <https://usqcd.lns.mit.edu/qlua>.
- [87] V. Bernard, H. W. Fearing, T. R. Hemmert, and U.-G. Meißner, Nucl. Phys. A **635**, 121 (1998), arXiv:hep-ph/9801297.
- [88] T. R. Hemmert and W. Weise, Eur. Phys. J. A **15**, 487 (2002), arXiv:hep-lat/0204005.